RIM-Binding Protein 2 organizes Ca^{2+} channel topography and regulates release probability and vesicle replenishment at a fast central synapse

1 **Tanvi Butola[1,2,3,4*], Theocharis Alvanos[1,2,3,4,*], Anika Hintze[1,4,5], Peter Koppensteiner[6], David**

2 **Kleindienst[6], Ryuichi Shigemoto[6], Carolin Wichmann[1,4,5,7], Tobias Moser[1,2,4,7]**

3 [1]Institute for Auditory Neuroscience (IAN) and InnerEarLab, University Medical Center Göttingen,

4 37075 Göttingen, Germany

5 [2]Synaptic Nanophysiology Group, Max Planck Institute for Biophysical Chemistry Göttingen, Germany

6 [3]International Max Planck Research School for Neurosciences and Göttingen Graduate Center for

7 Neurosciences, Biophysics, and Molecular Biosciences (GGNB), University of Göttingen, Germany

8 [4]Collaborative Research Center 1286, University of Göttingen, Göttingen, Germany

9 [5]Molecular Architecture of Synapses Group, IAN and Center for Biostructural Imaging of

10 Neurodegeneration (BIN), Göttingen, Germany

11 [6]Molecular Neuroscience Group, Institute for Science and Technology Austria (IST), Klosterneuburg,

12 Austria

13 [7]Cluster of Excellence "Multiscale Bioimaging: from molecular machines to networks of excitable

14 cells", University of Göttingen, 37075 Göttingen, Germany

15 **Correspondence:** Tobias Moser, tmoser@gwdg.de

16 **Main Figures**: 10, **Extended Data Figures**: 8, **Tables**: 7

17   **Words**: Abstract: 242, Significance Statement: 110, Introduction: 638, Discussion: 1544

18   **Keywords:** cochlear nucleus, calyceal synapse, short-term plasticity, readily releasable pool, active

19   zone topography, Ca^{2+} influx-exocytosis coupling

20   **Running title:** RIM-BP2 promotes vesicular release and replenishment

21   **Author Contribution**

22   This study was conceived by T.M. and T.B. The experimental work was performed by T.B. (slice

23   electrophysiology, *in vivo* electrophysiology, electron microscopy in the lab of R.S. with help of P.K.,

24   D.K. and R.S.), T.A. (slice electrophysiology, immunohistochemistry) and A.H. (electron microscopy).

25   T.M., T. A., and T.B. prepared the manuscript with contributions of A.H. and C.W.

26   **Acknowledgements**

36   **Conflict of interest**

37   The authors declare no conflict of interest.

38

2

Abstract

RIM-Binding Protein 2 (RIM-BP2) is a multi-domain protein of the presynaptic active zone (AZ). By binding to Rab-interacting protein (RIM), bassoon and voltage-gated Ca^{2+} channels (Ca_V), it is considered to be a central organizer of the topography of Ca_V and release sites of synaptic vesicles (SVs) at the AZ. Here, we investigated the role of RIM-BP2 at the endbulb of Held synapse of auditory nerve fibers with bushy cells of the cochlear nucleus, a fast relay of the auditory pathway with high release probability. Disruption of RIM-BP2 lowered release probability altering short-term plasticity and reduced evoked excitatory postsynaptic currents (EPSCs). Analysis of SV pool dynamics during high frequency train stimulation indicated a reduction of SVs with high release probability but an overall normal size of the readily releasable SV pool (RRP). The Ca^{2+}-dependent fast component of SV replenishment after RRP depletion was slowed. Ultrastructural analysis by super-resolution light and electron microscopy revealed an impaired topography of presynaptic Ca_V and a reduction of docked and membrane-proximal SVs at the AZ. We conclude that RIM-BP2 organizes the topography of Ca_V, and promotes SV tethering and docking. This way RIM-BP2 is critical for establishing a high initial release probability as required to reliably signal sound onset information that we found to be degraded in bushy cells of RIM-BP2-deficient mice *in vivo*.

Significance Statement

RIM-binding proteins (RIM-BPs) are key organizers of the active zone (AZ). Using a multidisciplinary approach to the calyceal endbulb of Held synapse that transmit auditory information at rates of up to hundreds of Hertz with sub-millisecond precision we demonstrate a requirement for RIM-BP2 for normal auditory signaling. Endbulb synapses lacking RIM-BP2 show a reduced release probability despite normal whole-terminal Ca^{2+} influx and abundance of the key priming protein Munc13-1, a

61   reduced rate of SV replenishment, as well as an altered topography of $Ca_V2.1$ Ca^{2+} channels, and fewer

62   docked and membrane proximal synaptic vesicles. This hampers transmission of sound onset

63   information likely affecting downstream neural computations such as of sound localization.

4

64   **Introduction**

65   Active zones (AZs) are specialized regions at the presynaptic terminals where neurotransmitter

66   release occurs. AZs employ a sophisticated machinery to enable ultrafast coupling of the incoming

67   action potential to the release of transmitter via Ca^{2+}-triggered SV fusion. Voltage-gated Ca^{2+} channels

68   (Ca_V) and SV release sites represent the core machinery, and their relative topography at the AZ co-

69   determines the release probability (recent reviews in: Kaeser and Regehr, 2014; Schneggenburger

70   and Rosenmund, 2015; Walter et al., 2018; Dittman and Ryan, 2019). The function and abundance of

71   Ca_V (recent reviews in: Pangrsic et al., 2018; Dolphin and Lee, 2020) is positively regulated by auxiliary

72   subunits and multi-domain proteins of the AZ such as RIM-BP, RIM, piccolo, bassoon, CAST and ELKS.

73   Several of these proteins promote the clustering of Ca^{2+} channels at the AZ and/or their

74   interaction with the SV release sites (Gundelfinger and Fejtova, 2012; Südhof, 2012; Moser et al.,

75   2019). RIM and RIM-BPs, in particular, have been considered as molecular linkers of Ca_V and vesicular

76   release sites. Direct and indirect interactions of RIMs with Ca_V are well established (Kiyonaka et al.,

77   2007; Gebhart et al., 2010; Kaeser et al., 2011; Picher et al., 2017). Proline-rich sequences of RIMs

78   have been shown to bind the SH3-domains of RIM-BP that directly interacts with Ca_V (Hibino et al.,

79   2002; Kaeser et al., 2011). Deletion of *Drosophila* RIM-BP disrupted Ca_V clustering at the AZs of larval

80   neuromuscular junctions consequently impairing their functional coupling to SV release: altered

81   short-term plasticity demonstrating a reduced release probability (Liu et al., 2011). Of the three

82   mammalian RIM-BP isoforms, RIM-BP1 and 2 are neuron-specific, whereby RIM-BP2 seems to be the

83   isoform that is most relevant for transmission at conventional synapses (Acuna et al., 2015; Grauel et

84   al., 2016). Disruption of RIM-BP1 and 2 did not alter the Ca^{2+} current at the calyx of Held synapse

85   (Acuna et al., 2015), while lack of RIM-BP2 (Krinner et al., 2017; Luo et al., 2017) and of RIM-BP1 (Luo

86   et al., 2017) reduced the Ca_V number at ribbon-type AZs. An alteration of the Ca_V topography at the

87 AZs has been reported based on super-resolution immunofluorescence microscopy (Grauel et al.,

88 2016; Krinner et al., 2017).

89   A loosening of the otherwise tight spatial relationship of Ca_V and SV release sites was indicated

90 by the reduced release probability and a greater sensitivity to the intracellular presence of the "slow"

91 Ca^{2+} chelator EGTA in the absence of RIM-BP(1)/2 (Acuna et al., 2015; Grauel et al., 2016; Luo et al.,

92 2017). A similar conclusion was reached in sensory hair cells where, unlike in CNS synapses, SV

93 replenishment was impaired in the absence of RIM-BP2 (Krinner et al., 2017). However, in contrast

94 to the dramatic impairment of synaptic transmission at RIM-BP deficient neuromuscular junctions in

95 *Drosophila* (Liu et al., 2011), transmission was affected more subtly by RIM-BP deletion at mammalian

96 synapses (Acuna et al., 2015; Grauel et al., 2016; Krinner et al., 2017; Luo et al., 2017). This might

97 relate to partial compensation by other candidate linkers of Ca_V and SV release sites such as long RIM

98 isoforms (Acuna *et al*, 2016). Recently, two alternative actions of RIM-BPs were indicated based on

99 molecular perturbations studies in hippocampal neurons: i) binding to Ca_V enabling their tight

100 coupling to SVs or ii) promoting SV priming by interaction with Munc13-1 (Brockmann et al., 2020).

101 Here we aimed to further characterize the function of RIM-BP2 at the endbulb of Held synapse, the

102 first central auditory synapse (von Gersdorff and Borst, 2002; Yu and Goodrich, 2014), that employs

103 high vesicular release probability at its more than 100 AZs for reliable and temporally precise signal

104 transmission from auditory nerve fibers (ANFs) to bushy cells (BCs) at frequencies of hundreds of

105 Hertz (Trussell, 1999; Wang et al., 2011). We combined electrophysiological analysis with studies of

106 the molecular composition and ultrastructure of the AZ in RIM-BP2-deficient endbulbs.

107

108

Materials and Methods

Animals

The constitutive RIM-BP2 knockout (RIM-BP2 KO) mice were described in (Grauel et al., 2016) and

kindly provided to us by Drs. Christian Rosenmund, Katharina Grauel and Stephan Sigrist. All

experiments were performed in compliance with the guidelines of the German animal welfare act

and were approved by the board for animal welfare of the University Medical Center Göttingen and

the animal welfare office of the state of Lower Saxony.

Slice electrophysiology

Slice preparation: Acute parasagittal slices (150μm) from the anteroventral cochlear nucleus (aVCN)

were obtained as described previously (Mendoza Schulz et al., 2014). Briefly, after sacrifice by

decapitation, brains were dissected out and quickly immersed in ice-cold low Na^+ and low Ca^{2+} cutting

solution containing (in mM): 50 NaCl, 26 $NaHCO_3$, 120 sucrose, 1.25 $NaH_2PO_4.H_2O$, 2.5 KCl, 20 glucose,

0.2 $CaCl_2$, 6 $MgCl_2$, 0.7 Na L-ascorbate, 2 Na pyruvate, 3 myo-inositol, 3 Na L-lactate with pH adjusted

to 7.4 and osmolarity of around 310 mOsm/l. After removal of the meninges from the ventral face of

the brainstem, the two hemispheres were separated by a midsagittal cut and the forebrain was

removed at the pons-midbrain junction. The brain blocks containing brain stem and cerebellum were

then glued (cyanoacrylate glue; Loctite 401, Henkel) to the stage of a VT 1200S vibratome (Leica

microsystems, Wetzlar, Germany) such that the medial side was glued on, the ventral side was facing

the blade and the lateral side was facing upwards, submerged in ice-cold cutting solution. For

sectioning, the blade was positioned at the height of cerebellar flocculus and sections were cut at a

blade feed rate of 0.02 mm/s with an amplitude of 1.50 mm. Slices were incubated for 30min in

artificial cerebrospinal fluid (aCSF) maintained at 35°C, and then kept at room temperature (22-24°C)

131   until recording. Composition of aCSF was identical to the cutting solution except (in mM): 125 NaCl,

132   13 glucose, 2 $CaCl_2$ and 1 $MgCl_2$. The pH of the solution was adjusted to 7.4 and osmolarity was around

133   310 mOsm/l. All solutions were continuously aerated with carbogen (95% O_2, 5% CO_2). For

134   presynaptic endbulb recordings, coronal sections were made instead of parasagittal as described

135   above. The only difference was that after the forebrain was removed at the pons-midbrain junction,

136   the dissected brain was not cut midsagitally and the brain block containing the brain stem and the

137   cerebellum was then glued to the vibratome stage with the caudal aspect facing upwards and the

138   ventral side towards the blade.

139   Electrophysiology: Patch-clamp recordings were made from BCs of aVCN using EPC10 USB Patch

140   clamp amplifier controlled by the Patchmaster software (HEKA Elektronik, Lambrecht/Pfalz,

141   Germany). Sampling interval and filter settings were 25 μs and 7.3 kHz respectively. Cells were

142   visualized by differential interference contrast (DIC) microscopy through a 40x water-immersion

143   objective (NA 0.8; Zeiss, Oberkochen, Germany) using an Axioscope 2 FS plus microscope (Zeiss). All

144   experiments were conducted at a temperature of 33-35°C, maintained by constant superfusion (flow

145   rate 3-4 ml/min) of aCSF, heated by an inline solution heater (SH-27B with TC-324B controller; Warner

146   Instruments, Hamden, CT, USA) and monitored by a thermistor placed between the inflow site and

147   the slice, in the recording chamber.

148   Patch pipettes were pulled with P-87 micropipette puller (Sutter Instruments Co., Novato, CA, USA)

149   from borosilicate glass capillaries with filament (GB150F, 0.86x1.50x80mm; Science Products,

150   Hofheim, Germany). Open tip pipette resistance was 1.5-3 MΩ when filled with intracellular solution

151   containing (in mM): 115 K-gluconate, 10 HEPES, 8 EGTA, 10 Na_2Phosphocreatine, 4 ATP-Mg, 0.3 GTP-

152   Na, 4.5 $MgCl_2$, 10 NaCl and 1 N-(2,6-dimethylphenyl carbamoylmethyl) triethylammonium chloride

153   (QX-314; Alomone Labs, Jerusalem, Israel) to block sodium channels, with a pH of 7.35 and an

8

154 osmolarity of 300 mOsm/l. Additionally, 1 mM of fluorescent dye Alexa-488 (Invitrogen) was added

155 to the recording pipette and cell structure was examined during experiments using a HXP 120 mercury

156 lamp, with FITC filter (Semrock hardcoat). Cells were voltage-clamped at a holding potential of −70

157 mV, after correction for a liquid junction potential of 12 mV. Mean series resistance was around 5

158 MΩ and was compensated up to 70% with a 10 μs lag. Presynaptic ANF were minimally stimulated

159 with a monopolar electrode in a patch pipette filled with aCSF, placed at a distance of at least three

160 cell diameters from the cell being recorded. Stimulating currents of 10-20 μA were delivered through

161 a stimulus isolator (A360 World Precision Instruments, Sarasota, FL, USA). For the main set of

162 recordings, bath solution (aCSF) was supplemented with: 1 mM kynurenic acid sodium salt (abcam

163 Biochemicals, Cambride, UK), a low-affinity AMPAR antagonist, to prevent receptor

164 saturation/desensitization, 100μM Cyclothiazide to prevent AMPAR desensitization, 10 μM

165 Bicuculline methchloride, a $GABA_A$ receptor antagonist and 2 μM Strychnine hydrochloride, a glycine

166 receptor antagonist.

167 For patch-clamp experiments at the endbulbs of Held patch-pipettes were coated with either dental

168 wax or Sylgard to minimize fast capacitive transients and stray capacitance during voltage clamp

169 experiments. Open tip pipette resistance was 4-5 MΩ with an intracellular solution containing (in

170 mM): 130 Cs-methanesulfonate, 20 TEA-Cl, 10 HEPES, 0.5 EGTA, 5 Na_2Phosphocreatine, 4 ATP-Mg,

171 0.3 GTP-Na, with pH adjusted to 7.3 with CsOH osmolarity of 320 mOsm/l. For anatomical

172 confirmation 1 mM of fluorescent dye Alexa-488 (Invitrogen) was added to the recording pipette. The

173 bath solution differed from the aCSF normally used (in mM): 85 NaCl, 25 glucose, 2 $CaCl_2$ and 1 $MgCl_2$.

174 The pH of the solution was adjusted to 7.4 and osmolarity was around 310mOsm/l. Additionally, the

175 bath solution was supplemented with 1 μM TTX, 1 mM 4-AP, and 40 mM TEA-Cl to suppress voltage-

176 gated Na^+ and K^+ currents. Presynaptic terminals were voltage-clamped at a holding potential of −80

177   mV, a liquid junction potential of 3 mV was ignored. Series resistance was <30 MΩ and was

178   compensated up to 50% with a 10 µs lag.

179   **Systems physiology: Extracellular recordings from single bushy cells**

180   Extracellular recordings from single units of bushy cells (BCs) in the aVCN were performed as

181   described before (Jing et al., 2013; Strenzke et al., 2016) on 9 to 10-week-old mice. After anesthetizing

182   the mice with i.p. injection of urethane (1.32 mg/kg), xylazine (5 mg/kg) and buprenorphine (0.1

183   mg/kg), a tracheostomy was performed, their cartilaginous ear canals were removed and then they

184   were positioned in a custom-designed head-holder and stereotactic system. After partial removal of

185   the occipital bone and cerebellum to expose the surface of the cochlear nucleus, a glass

186   microelectrode was advanced through the anterior portion of the aVCN to avoid the auditory nerve

187   fibers and instead target the area with a higher fraction of spherical BCs. Acoustic stimulation was

188   provided by an open field Avisoft ScanSpeak Ultrasonic Speaker (Avisoft Bioacoustics). "Putative"

189   spherical BCs were identified and differentiated from other cell types in the cochlear nucleus by their

190   characteristic 'Primary-like' peristimulus time histogram (PSTH) (Taberner and Liberman, 2005),

191   irregular firing pattern demonstrated by a ≥ 0.5 coefficient of variation of inter-spike intervals of

192   adapted responses, and a first spike latency of ≤ 5 ms. Bushy cells units were distinguished from

193   auditory nerve fiber (ANFs, also having 'Primary-like' PSTH) based on their stereotactic position (<1.1

194   mm below the surface of the cochlear nucleus). Recordings were performed using TDT system III

195   hardware and an ELC-03XS amplifier (NPI electronics).

196

197

198

199 **Immunohistochemistry and confocal imaging**

200 Mice at postnatal day 20-24 were deeply and terminally anesthetized with Xylazin (5 mg/kg) and

201 Ketamin (10 mg/ml) in 0.9% saline and then transcardially perfused with 2% freshly prepared ice-cold

202 paraformaldehyde with pH adjusted to 7.4. The fixed brain was then removed and brainstem was

203 dissected with a coronal cut few millimetres nasal to the junction between occipital cortex and

204 cerebellum. The brain block was washed overnight in 30% sucrose solution in PBS. For sectioning, the

205 brain block was embedded in Tissue Tek Cryomatrix (Thermo Fisher Scientific, Waltham, MA, USA)

206 and then fixed on the stage of the cryostat (Figocut E cryotome, Reichert-Jung, Depew, NY, USA) such

207 that the caudal aspect was facing upwards and the dorsal side was towards the blade. Advancing from

208 caudal to nasal, 30 μm coronal sections were cut (chamber temperature: -20°C, object temperature:

209 -22°C) and discarded until the appearance of the 7th cranial nerve. Subsequent sections containing

210 aVCN were collected onto electrostatically charged microscope slides (SuperFrost Plus, ThermoFisher

211 Scientific, MA, USA). For parallel processing, one slice of each genotype was collected per slide.

212 Thereafter, the slices were washed for 10 min in PBS and incubated in Goat Serum Dilution

213 Buffer (GSDB; 16% normal goat serum, 450 mM NaCl, 0.3% Triton X-100, 20 mM phosphate buffer,

214 pH 7.4) for 1 h, followed by incubation in primary antibodies diluted in GSDB, for 3 h, in a wet chamber

215 at room temperature. After washing 2x10 min with wash buffer (450 mM NaCl, 0.3% Triton X-100, 20

216 mM phosphate buffer) and 2x10 min with PBS, the slices were incubated with secondary antibodies

217 diluted in GSDB, for 1 h, in a light-protected wet chamber at room temperature. The slices were then

218 washed 2x10 min with wash buffer, 2x10 min with PBS and 1x10 min in 5 mM phosphate buffer, and

219 finally mounted with a drop of fluorescence mounting medium based on Mowiol 4-88 (Carl Roth,

220 Karlsruhe, Germany) and covered with a thin glass coverslip. The above described perfusion fixation

221 method was used to stain for RIM-BP2 (Figure 4 A, B). The remaining immunofluorescence

11

222   experiments (Munc13-1, RIM2, CAST, bassoon) were done on samples taken from RIM-BP2 KO mice

223   aged between p15 – p23 and WT littermates. After obtaining coronal sections from the cryostat the

224   slices were maintained frozen at -20°C until immersion fixation or fixed directly on ice in a solution of

225   PBS containing 3% w/v heat depolymerized PFA (70°C) for 3 minutes. This alternative method of

226   fixation showed robust labelling with less background than perfusion fixed samples labelled against

227   the same markers. For the comparison of $Ca_V2.1$ immunofluorescence levels in confocal microscopy

228   and the STED analysis of $Ca_V2.1$ and bassoon clusters, we used very brief fixation with 3% PFA for less

229   than one minute (30-40 seconds) as $Ca_V2.1$ labelling was impeded by stronger fixation. Thereafter,

230   the blocking and immunolabelling protocols were followed exactly as described above for the

231   perfusion fixed samples.

232   Primary antibodies used were: rabbit anti-RIM-BP2 (1:200), guinea pig anti-VGLUT1 (1:500), rabbit

233   anti-VGLUT1 (1:1000), mouse anti-gephyrin (1:500), mouse anti-Sap7f407 to bassoon (1:500; Abcam,

234   Cambridge, UK), guinea pig anti-bassoon (1:500), rabbit anti-Munc13-1 (1:200), rabbit anti-RIM1

235   (1:200), rabbit anti-RIM2 (1:200), rabbit anti-CAST (1:200), rabbit anti-P/Q Ca^{2+} channel (1:500),

236   chicken anti homer1 (1:200). Unless stated otherwise, primary antibodies were purchased from

237   Synaptic Systems, Göttingen, Germany. Secondary antibodies used were: AlexaFluor488-,

238   AlexaFluor568- and AlexaFluor647-labeled antibodies (1:200, Invitrogen), goat anti-guinea pig

239   STAR580 and goat anti-rabbit STAR 635p (1:200, Abberior GmbH, Goettingen, Germany).

240   Confocal images were acquired using a laser-scanning confocal microscope (Leica TCS SP5; Leica

241   Microsystems) equipped with 488 nm (Ar) and 561/633 nm (He-Ne) lasers and 63x/1.4 NA oil-

242   immersion objective. STED and confocal images ($Ca_V2.1$ and bassoon analyses) were acquired using

243   a 2-color STED microscope (Abberior Instruments, Göttingen, Germany) equipped with 561 and 640

244   nm excitation lasers, a 775 nm laser for STED (1.2W) and a 100x oil immersion objective (1.4NA,

245 Olympus). Confocal z-stacks were processed with Imaris (Bit-plane, Zurich, Switzerland) for spot

246 detection, co-localization analysis and fluorescence intensity calculation using custom Matlab scripts.

247 STED images of $Ca_V2.1$ and bassoon were analyzed using Igor Pro7 (Wavemetrics, Lake Oswego, OR,

248 USA). Samples of both genotypes: RIM-BP2 WT and RIM-BP2 KO were processed and imaged in

249 parallel, using same laser power, gain and microscope settings.

250 **SDS – Freeze-fracture Replica Immuno-Labelling (SDS-FRIL)**

251 Mice at postnatal day 20-24 were deeply and terminally anesthetized with Xylazin (5 mg/kg) and

252 Ketamin (10 mg/ml) in 0.9% saline, and perfused transcardially with ice-cold PBS followed by

253 perfusion with freshly-prepared 2% PFA with 15% saturated picric acid solution in 0.1 M phosphate

254 buffer (PB) with pH adjusted to 7.3. The fixed brain was then removed and brainstem was dissected

255 with a coronal cut few millimetres nasal to the junction between occipital cortex and cerebellum. The

256 brain block was washed over night in 30% sucrose solution in PBS. Coronal slices (130 μm thick) were

257 cut from the fixed brain block fusing a vibratome microslicer (Linear-Pro7, Dosaka) in ice-cold PBS.

258 The rostral anterior ventral cochlear nuclei were trimmed by hand from the slices. The trimmed

259 sections were then immersed in graded glycerol concentrations of 10%-20% at room temperature for

260 20 min each, followed by 30% at 4°C overnight. The trimmed sections were sandwiched between two

261 metal carriers and then rapidly frozen by a high-pressure freezing machine (HPM010, BAL-TEC,

262 Balzers). Using a freeze etching device (BAF060, BAL-TEC), frozen samples were then fractured into

263 two parts at -115°C, and the fractured faces were replicated by sequential deposition of carbon

264 (thickness: 5 nm from 90° angle), platinum (thickness: 2 nm from 60° angle, unidirectional), and

265 carbon again (thickness: 20 nm from 90° angle). After thawing, the tissue debris attached to the

266 replica was digested with gentle shaking at 80°C for 18 h, in a solution containing 2.5 % SDS, 20%

13

267   sucrose, and 15 mM of Tris-HCl with pH set to 8.3. The replicas were washed 3 x 10 min in wash buffer

268   (0.1% Tween-20, 0.05% BSA, 0.05% NaN$_3$ in TBS, pH 7.4), and then the non-specific binding sites were

269   blocked with 5% BSA in wash buffer for 1 h at 4°C.

270   For multiple immunolabelling against Ca$_V$2.1 and AZ proteins, replicas were first incubated with

271   guinea pig anti-Ca$_V$2.1 antibody (8 µg/ml in 1% BSA; Frontier Institute AB_2571851) at 15°C for 3 days,

272   then with anti-guinea pig secondary antibodies conjugated with 10 nm gold particles (1:30 diluted in

273   5% BSA; British Biocell International) at 15°C overnight, followed by incubation with a cocktail of

274   rabbit anti-AZ proteins antibodies (anti-ELKS at 2 µg/ml in 1% BSA; gift from Prof. Ohtsuka raised

275   against rat ELKS aa117-142, anti-Neurexin at 4 µg/ml in 1% BSA; gift from Prof. Watanabe raised

276   against aa1499-1507 and anti-RIM at 4 µg/ml in 1% BSA; Synaptic Systems 140203) at 15ºC overnight,

277   and finally with anti-rabbit secondary antibodies conjugated with 5 nm gold particles (1:30 diluted in

278   5% BSA; British Biocell International) at 15°C overnight. After immunolabelling, replicas were rinsed

279   three times with 0.05% BSA in TBS, washed with TBS and distilled water, and mounted on formvar-

280   coated copper grids.

281   The labelled replicas were imaged using a Tecnai-12 transmission electron microscope (FEI; AV 120

282   kV). To obtain a planar view for quantitative measurement of immuno-gold particle number and

283   densities, profile of synaptic structures (AZ and PSD) were tilted in the electron beam. IMP clusters

284   representing PSDs were manually demarcated and the area was measured using ImageJ software

285   (Rubio et al., 2017). Active zone areas were marked by hand with the experimenter being blinded to

286   the identity of the two genotypes. Quantitative analysis of immune-gold particles was done using an

287   in-house software tool – Gold Particle Detection and Quantification (Luján et al., 2018). To define

288   clusters of gold particles the threshold for the distance between particles belonging to the same

289   cluster was calculated as µ + 2σ, where µ and σ are the mean and standard deviation obtained from

14

290   a Gaussian fit to the distribution of nearest neighbour distances (NND) between particles. μ + 2σ was

291   43.02 nm and 43.92 nm for Ca$_V$2.1 gold particles in RIM-BP2 WT and KO respectively. We set the

292   threshold at 40 nm to match the value used in a previous analysis (Miki et al., 2017). The distances

293   between particles were measured from their centers of mass, and the minimum number of particles

294   required to form a cluster was set to three. We additionally compared our 'real' distribution of NNDs

295   between gold particles and their clustering to 500 random and fitted simulations (keeping the NNDs

296   between the simulated particles similar to the ones between the 'real' gold particles) generated by

297   Monte-Carlo simulations (as described in (Luján et al., 2018; Kleindienst et al., 2020)) to confirm that

298   the clusters visualized through our analysis are not generated by chance.

299   **High-pressure freezing, Freeze substitution and Electron tomography**

300   Parasagittal slices from cochlear nuclei were obtained as described for slice electrophysiology. Slices

301   containing the cochlear nucleus were trimmed and mounted onto type A specimen carriers (Leica

302   Microsystems, Wetzlar, Germany) filled with cutting solution. The flat side of the type B carriers (Leica

303   Microsystems, Wetzlar, Germany) was dipped in 1-hexadecene (Sigma-Aldrich, Wetzlar, Germany)

304   and placed onto the type A carriers. Samples were frozen immediately using a HPM100 (Leica

305   Microsystems, Wetzlar, Germany) and transferred into liquid nitrogen. Freeze-substitution was

306   performed in an EM AFS2 (Leica Microsystems, Wetzlar, Germany) according to Wong *et al.* (Wong

307   et al., 2014). The slices were incubated in 0.1% (w/v) tannic acid in acetone at −90°C for 4 days and

308   afterward washed three times for 1 h each in acetone at −90°C. 2% (w/v) osmium tetroxide in acetone

309   was applied and incubated for 40.4 h. During that time the temperature was raised slowly to 4°C

310   (10°C/h). At 4°C, osmium tetroxide was removed, and the samples were washed with acetone three

311   times and brought to room temperature. Slices were infiltrated in epoxy resin (Agar-100 kit, Plano,

312   Germany; epoxy/acetone 1:1 3-6 h; 100% epoxy overnight). Finally, samples were further incubated

313   in fresh 100% epoxy and placed in embedding molds.

314   After polymerization for 48 h at 70°C, excess resin was removed with a fine file (DiAtome, Switzerland)

315   and the block was trimmed to a pyramid using a razor blade. To check the region and the structural

316   preservation, 65 nm ultrathin sections were cut with a diamond knife (DiAtome, Switzerland) using

317   an EM UC7 (Leica Microsystems, Wetzlar, Germany) ultramicrotome. Sections were collected on

318   formvar-coated copper slot grids (Athene, Plano, Wetzlar, Germany, for ultrathin sections). For

319   electron tomography, 250 nm semi-thin sections were obtained and collected on mesh grids (100

320   mesh; Athene, Plano, Wetzlar, Germany, for semi-thin sections). Post-staining was performed with

321   Uranyless (EMS, Hatfield, PA) for 20 min.

322   The region and quality of the tissue was checked at 80 kV using a JEM1011 transmission electron

323   microscope (JEOL, Freising, Germany) equipped with a GatanOrius 1200A camera (Gatan, Munich,

324   Germany). Electron tomography was performed as described previously (Wong et al., 2014). 10 nm

325   gold beads (British Bio Cell/Plano, Germany) were applied to both sides of the stained grids. Big

326   synaptic terminals on bushy cells were identified and tilt series from endbulb AZs were acquired at

327   200 kV using a JEM2100 transmission electron microscope (JEOL, Freising, Germany) mostly from

328   −60° to +60° with a 1° increment at 15,000× using the Serial-EM software package with an image pixel

329   size of 0.95 nm (Mastronarde, 2005). Tomograms were generated using the IMOD package etomo

330   (Kremer et al., 1996).

331   Only asymmetric synapses with clearly identifiable PSDs were analyzed. However, in high-pressure

332   frozen samples, PSDs appear less electron-dense compared to chemical fixed synapses. Only AZs that

333   showed a PSD and a clear synaptic cleft, originating from large presynaptic terminals were analyzed

334   to exclude inhibitory synapses.

16

335 Tomograms were segmented semi-automatically using 3dmod (Kremer et al., 1996). The AZ

336 membrane was manually segmented every 15 virtual sections for five consecutive virtual sections

337 and then interpolated across the Z-stack, following the extent of the PSD and the parallel synaptic

338 cleft. Moreover, virtual sections were corrected manually after interpolation. The total surface area

339 of this object was then divided by two to calculate the AZ area.

340 Synaptic vesicles (SVs) were reconstructed at their maximum projection and the sphere size was

341 adjusted for each vesicle. The smallest distances from the outer leaflet of the SV membrane to the

342 inner leaflet of the AZ membrane were measured and SVs in contact with the AZ membrane were

343 defined as morphological docked SVs (0-2 nm distance). Moreover, all vesicles within 200 nm of the

344 AZ were quantified and categorized in 20 nm bins. The radii of the SVs were determined with the

345 program "imodinfo" of the IMOD software package and the diameters were calculated. For

346 quantification of lateral distances of docked SVs, models of tomogram top-views with docked SVs

347 were imported in ImageJ and the center of the captured AZ area was defined by setting two diagonal

348 lines from respective edges of the AZ. The crossing point was defined as the center and the distances

349 were measured from the outer membrane of the SV towards the center point.

350

351 **Data analysis**

352 Electrophysiology data were analyzed using Igor Pro (Wavemetrics, Lake Oswego, OR, USA), Mini

353 Analysis (Synaptosoft Inc., Fort Lee, NJ, USA) and GraphPad Prism software (La Jolla, CA, USA).

354 Synaptic delay was calculated as the time between the start of stimulus (voltage output of the

355 amplifier as dictated by the experiment protocol) and the time when the respective EPSC response

356 reached 10% of its peak amplitude.

357   Confocal images were analyzed using ImageJ software, Imaris (Bitplane AG, Zurich, Switzerland) and

358   Matlab (Mathworks). STED images of $Ca_V2.1$ channels were analysed using custom Igor pro scripts.

359   Single plane slices of the top (coverslip proximal) and/or bottom (distal from coverslip) membranes

360   of BCs were imaged to capture the $Ca_V2.1$ spots on a flat surface top view and enable 2D Gaussian

361   fitting. The $Ca_V2.1$ spots that were simultaneously closely juxtaposed to puncta of both homer1 and

362   bassoon were fitted with Igor Pro's 2D Gaussian function. Figures were assembled for display using

363   Adobe Illustrator (Adobe Systems, Munich, Germany). Unless reported otherwise, statistical

364   significance between groups was determined by either unpaired Student's t-test (in case of normally

365   distributed data with comparable variances between the groups) or Wilcoxon rank sum test (when

366   data distribution did not satisfy the criteria). Normality of distribution was tested with Jarque-Bera

367   test and variances were compared with F-test. Data were presented as mean ± S.E.M. when

368   compared using Student's t-test. In case of Wilcoxon's rank sum test, data were presented as box and

369   whisker plots showing grand median (of the means of all recordings), lower/upper quartiles, 10-90th

370   percentiles). *, **, ***, **** indicate p < 0.05, 0.01, 0.001 and 0.0001 respectively.

18

371   **Results**

372   **Deletion of RIM-BP2 impairs synchronous transmitter release at the endbulb of Held synapse**

373   To determine the functional role of RIM-BP2, we studied synaptic transmission at the endbulb of Held

374   synapse in acute parasagittal slices of the brainstem of constitutive RIM-BP2 knockout mice (RIM-BP2

375   KO, (Grauel et al., 2016)) recording spontaneous (no stimulation, no TTX applied) and evoked

376   excitatory postsynaptic currents (sEPSCs and eEPSCs, respectively) from bushy cells (BCs) of the

377   anteroventral cochlear nucleus (aVCN, Fig. 1A) at postnatal days 15-21. eEPSCs were elicited by

378   minimal electrical stimulation of the presynaptic ANF by a monopolar electrode placed in the

379   proximity (~3 cell diameters away) of the recorded BC, whereby each stimulus is aimed to elicit one

380   action potential in one endbulb (Yang and Xu-Friedman, 2008).

381   Experiments of Figure 1 were performed in the presence of 1 mM kynurenic acid and 100 µM

382   Cyclothiazide (CTZ) to avoid saturation and desensitization of AMPA receptors (Chanda and Xu-

383   Friedman, 2010), respectively. The concentration of CTZ used here, was adopted from previous

384   reports at the calyx of Held (Sakaba and Neher, 2001; Thanawala and Regehr, 2013). The former study

385   (Sakaba & Neher, 2001) examined the NMDA current in the presence of 100 µM CTZ and found no

386   evidence for a presynaptic CTZ effect at the calyx of Held. The eEPSC amplitude was reduced in RIM-

387   BP2 KO BCs as compared to littermate wildtype (WT, Fig. 1B-C, 3.50 ± 0.37 nA (KO) vs. 5.48 ± 0.73 nA

388   (WT), p = 0.022, Mann-Whitney U-test). There was a tendency towards slower eEPSC kinetics, but this

389   did not reach significance for either synaptic delay (Fig. 1D) or rise and decay time (Fig. 1E-G), (p-value

390   ≥ 0.05, Mann-Whitney U-test). EPSC recordings in the absence of kynurenic acid and CTZ (Fig. 1-1)

391   confirmed the eEPSC reduction, eliminating the possibility of CTZ obscuring the changes in AMPA

392   receptor composition or inducing membrane potential changes. The eEPSC kinetics was significantly

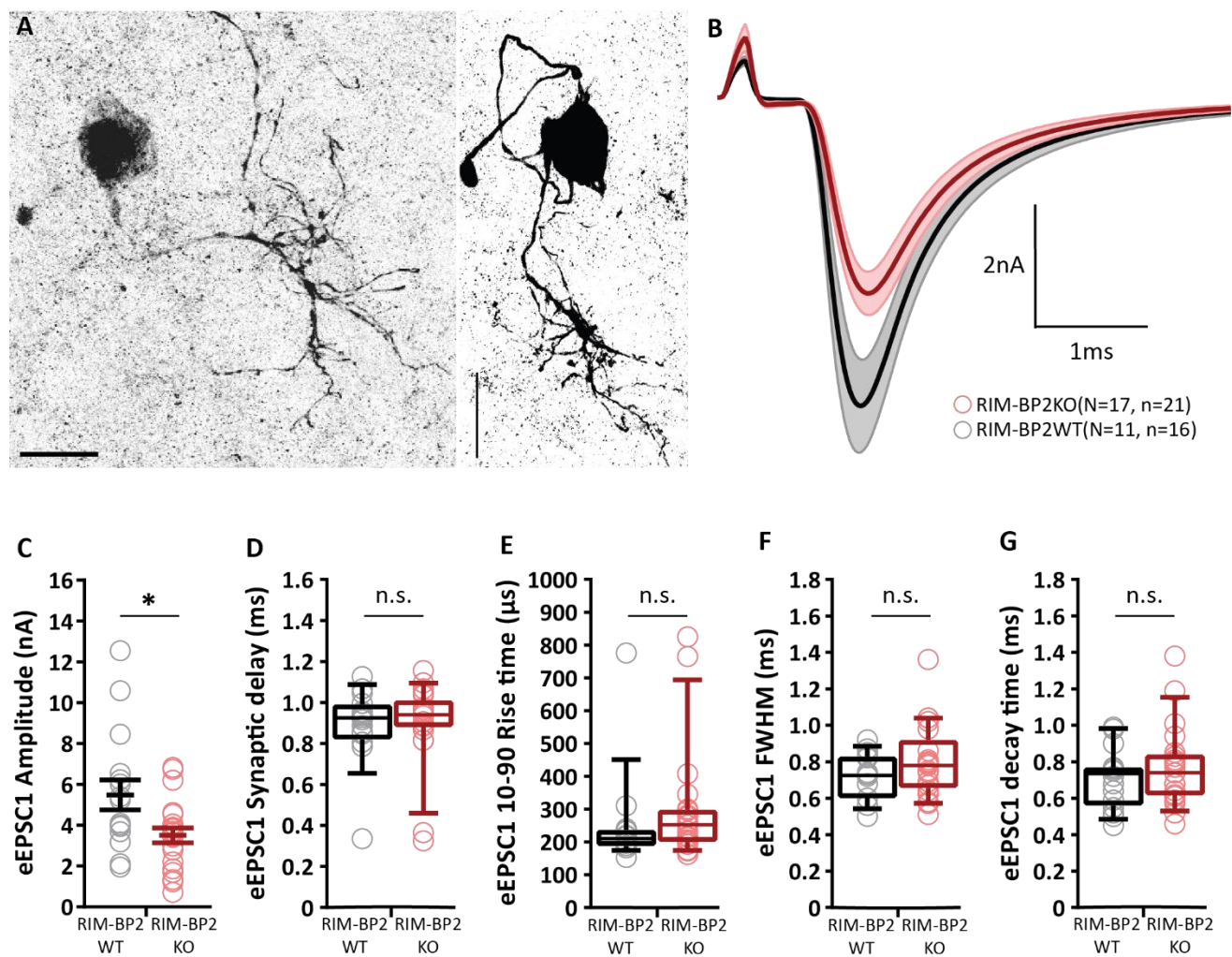393   slower for RIM-BP2 KO BCs under these conditions (Fig. 1-1).

19

Figure 1. Reduced amplitude of evoked EPSCs in RIM-BP2 deficient endbulb synapses.

(**A**) BCs (left and right panels showing dye-filled BCs) were distinguished from stellate cells (another major cell type in the aVCN) by the faster kinetics of their postsynaptic currents (Isaacson and Walmsley, 1995) and their characteristic short-term plasticity (Chanda and Xu-Friedman, 2010). In addition to such functional identification, each recorded cell was filled with fluorescent dye Alexa 488 via the patch pipette for morphological distinction. BCs are spherical in appearance with one primary dendrite terminating in a dense bush-like dendritic tree (Wu and Oertel, 1984), distinct from stellate cells, which are asymmetrical in shape and have multiple dendrites branching off in various directions giving them a star-like appearance. Scale bars: 20 µm. (**B**) Average traces (± SEM) of eEPSCs in RIM-BP2 KO (red) and WT (black) endbulbs. (**C**) Reduced eEPSC amplitude in RIM-BP2 KO compared to WT. (**D-G**) No significant differences in eEPSC kinetics: (**D**) synaptic delay, (**E**) 10-90% rise time, (**F**) full width at half-maximum and (**G**) decay time. Data points represent the mean estimate of each BC included in the analysis. Normality was tested with the Jarque-Bera test. Normally distributed data (**C**) are shown as grand mean (of the means of all BCs) ± SEM. Non-normally distributed data (**D, E, F, G**) are presented as box and whisker plots (grand median of all BC means, lower/upper quartiles, 10-90th percentiles); n.s. *p-value* ≥ 0.05, Mann-Whitney U-test. *N*: number of animals, *n*: number of BCs.
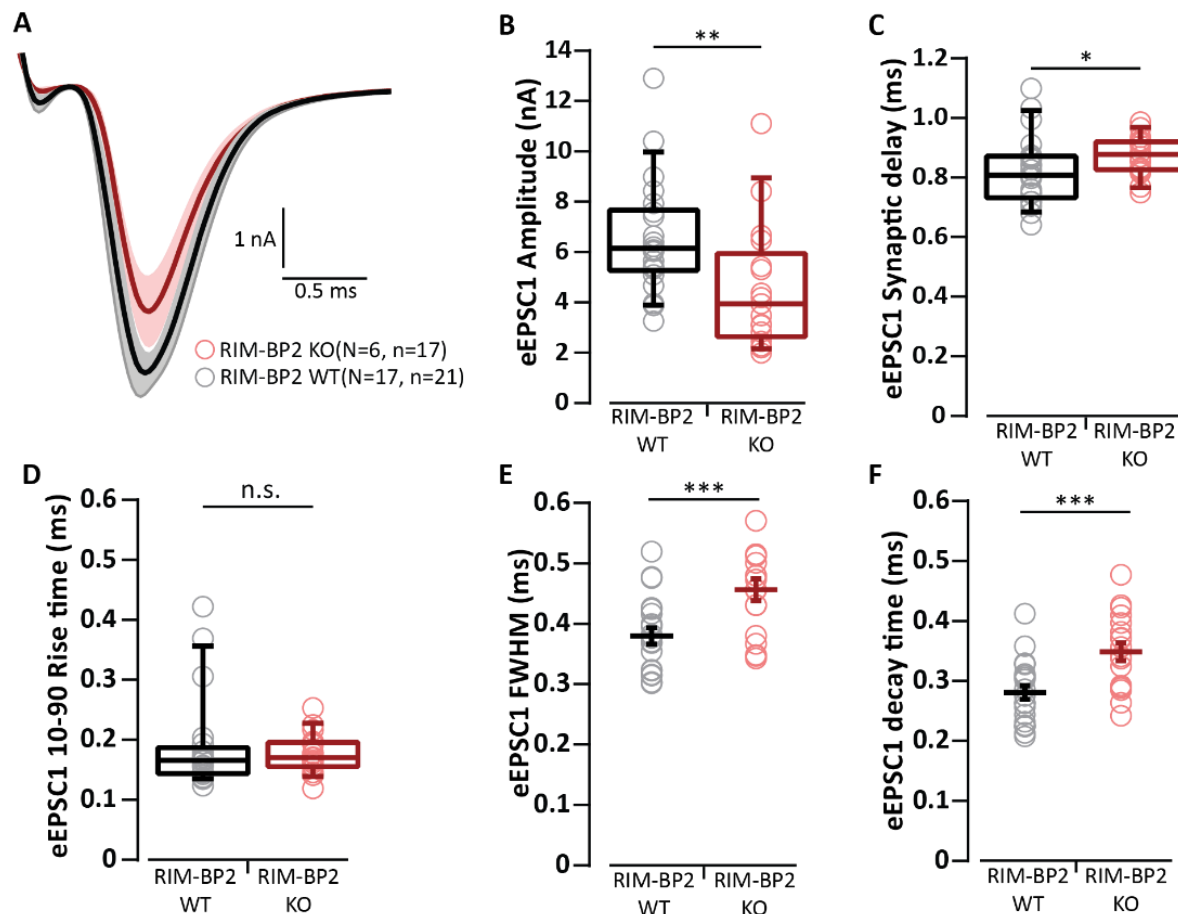
20

Figure 1-1. Evoked EPSC recordings in the absence of kynurenic acid and CTZ

(**A**) Average traces (± SEM) of eEPSCs in RIM-BP2-KO (red) endbulbs and WT (black) in the absence of kynurenic acid and CTZ. (**B**) Reduced eEPSC amplitude in RIM-BP2 KO compared to in WT. (**C-F**) eEPSC kinetics: (**C**) a larger synaptic delay, (**D**) unchanged 10-90% rise time, (**E**) wider full-width at half-maximum, and (**F**) slower decay time. Data points represent the mean estimate of each BC included in the analysis. Normality was tested with the Jarque-Bera test. Normally distributed data (**E, F**) are shown as grand mean (of the means of all BCs) ± SEM, and significance was tested with Student's t-test. Non-normally distributed data (**B, C, D**) are presented as box and whisker plots (grand median of all BC means, lower/upper quartiles, 10-90th percentiles), and significance was tested with Mann-Whitney U-test; n.s. *p-value ≥ 0.05, * p-value < 0.05, **p-value <0.01, *** p-value <0.001. N*: number of animals, *n*: number of BCs.

In order to test for potential changes in the quantal release properties we recorded spontaneous

EPSCs (sEPSCs) from BCs (Fig. 1-2). We did not observe differences in the sEPSC amplitude (Fig. 1-2A-

C), kinetics (Fig. 1-2D-F) and frequency (Fig. 1-2G; p-value ≥0.05 for all 3 quantities), which was also

the case when recording in the absence of kynurenic acid and CTZ (Table 1). Unaltered sEPSCs suggest

21

428 that the properties of single SV release and of postsynaptic glutamate response are intact in RIM-BP2

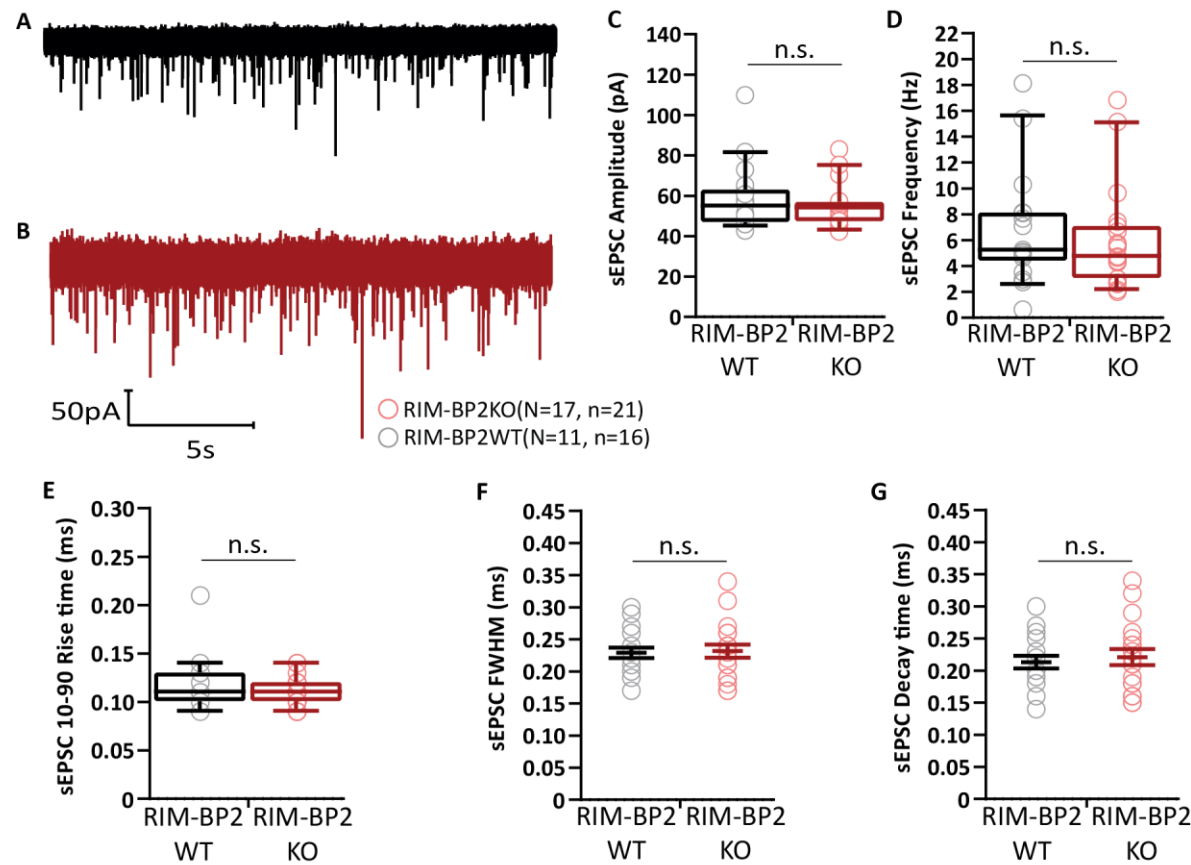429 deficient endbulb synapses at BCs.

430

Figure 1-2. Unaltered amplitude, kinetics and frequency of spontaneous EPSCs in RIM-BP2 deficient endbulb synapses

(**A, B**) Representative sEPSCs at WT (**A**, black) and RIM-BP2 KO (**B**, red) endbulbs of held: continuous traces are shown. No significant differences in (**C**) amplitude, (**D**) frequency, (**E**) 10-90% rise time, (**F**) full-width at half-maxima and (**G**) decay time in RIM-BP2 deficient endbulbs. sEPSC were recorded while intracellularly blocking BC action potential generation with QX-314. Each data point represents the mean estimate of each BC included in the analysis. Normality was tested with the Jarque-Bera test. Normally distributed data are depicted as mean (grand average of all BC means) ± SEM (**F, G**; n.s. p-value ≥ 0.05, unpaired Student's t-test). Non-normally distributed data are presented as box and whisker plots (grand median of all BC means, lower/upper quartiles, 10-90th percentiles) (**C, D, E**); n.s. p-value ≥ 0.05, Mann-Whitney U-test N: number of animals, n: number of BCs.

442

Parameter	WT	RIM-BP2 KO	p-value
Amplitude (pA)	130.54 ± 12.06	112.48 ± 4.03	0.22
10-90% Rise time (ms)	0.09 ± 0.003	0.09 ± 0.002	0.85
FWHM (ms)	0.18 ± 0.008	0.19 ± 0.004	0.46
Decay time (ms)	0.16 ± 0.010	0.17 ± 0.005	0.36
Frequency (Hz)	7.65 ± 1.28	8.01 ± 1.09	0.83

443 **Table 1. Unaltered sEPSC at the RIM-BP2 deficient endbulb of Held in the absence of kynurenic acid**
444 **and CTZ**
445 Data presented as mean (grand average of the means of all BCs) ± S.E.M. Statistical significance
446 between groups was determined by either unpaired Student's t-test (in case of normally distributed
447 data with comparable variances between the groups) or Mann-Whitney U-test (when data
448 distribution did not satisfy the criteria). Normality of distribution was tested with Jarque-Bera test
449 and variances were compared with F-test. WT N = 4; n = 10, RIM-BP2 KO N = 7; n = 19 (N, number of
450 animals; n, number of BCs).

451 Quantal size being unaltered, the reduced eEPSC alteration could result from either: (i) an impaired

452 stimulus-secretion coupling due to reduced Ca^{2+} influx and/or altered topography of Ca^{2+} channels

453 (Krinner et al., 2017) and fusion competent SVs (Acuna et al., 2015; Grauel et al., 2016; Luo et al.,

454 2017), or (ii) due to an impaired SV priming that has recently been shown to involve RIM-BP2

455 interaction with Munc13-1 (Brockmann 2020). We first checked for changes in presynaptic Ca^{2+} influx

456 in the absence of RIM-BP2 using ruptured-patch recordings from the endbulb of Held (Lin et al., 2011)

457 in mice after the hearing onset (postnatal days 13-16, Fig. 2). We did not observe significant changes

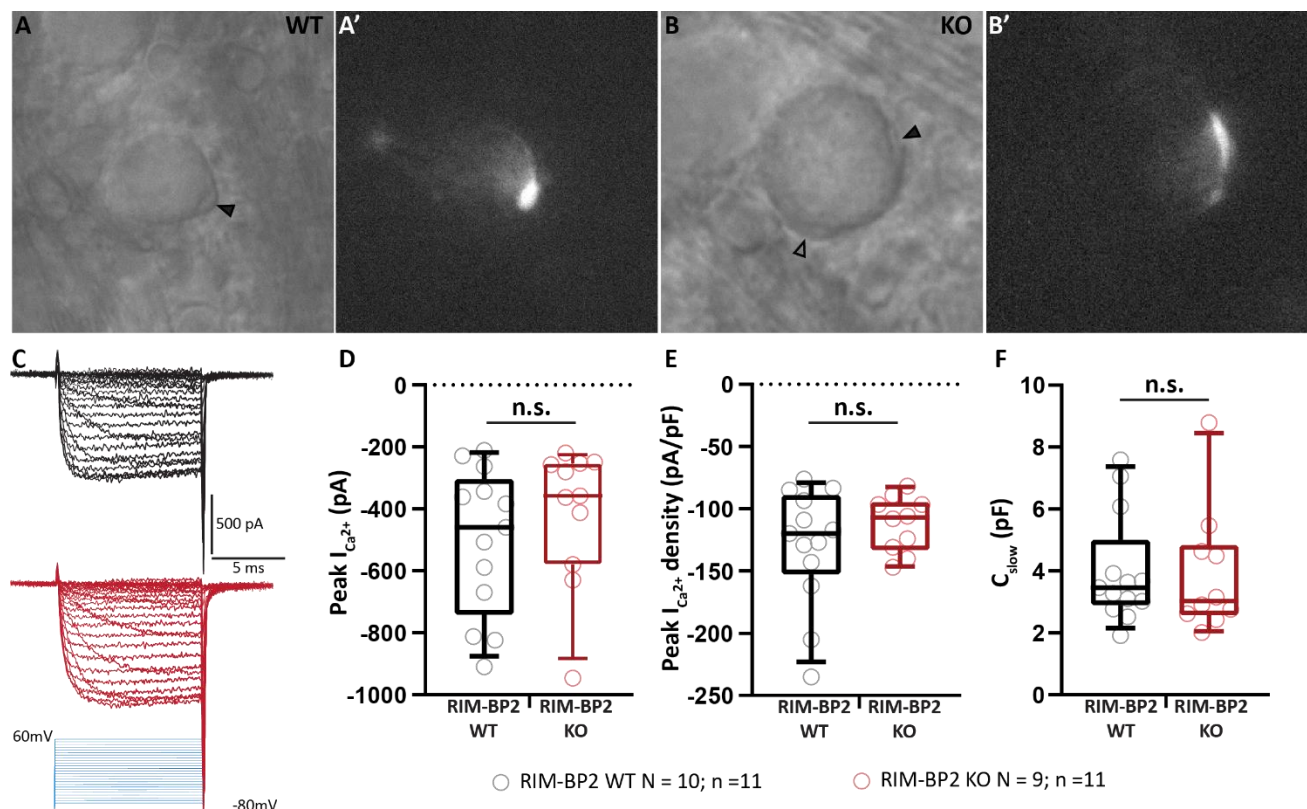458 in the peak Ca^{2+} current amplitude or peak Ca^{2+} current density in KO endbulbs of Held (Fig. 2).

459

23

460 **Figure 2. Ca^{2+} influx is unaltered in RIM-BP2 deficient endbulbs.**
461 (**A, B**) Bright-field images of the WT (**A**) and RIM-BP2 KO (**B**) bushy cells under DIC. The recorded
462 endbulb is demarcated by a solid black arrow head (**A, B**), while another endbulb onto to the same
463 bushy cell is shown by an open black arrowhead (**B**). Each recorded endbulb was filled with Alexa 488
464 to confirm that only the presynaptic terminal was accessed, and not the postsynaptic cell. Fluorescent
465 endbulbs are shown in **A', B'**. (**C**) Representative traces of presynaptic Ca^{2+} currents in WT (black) and
466 RIM-BP2 KO (red) in response to stepped increase in holding potential (stimulus protocol in blue). (**D-**
467 **F**) No significant difference was observed between the two genotypes in the peak Ca^{2+} current (**D**),
468 peak Ca^{2+} density (**E**; peak current/C$_{slow}$), and the size of the endbulb (**F**, estimated by C$_{slow}$). Each data
469 point represents the mean estimate of each endbulb included in the analysis. Normality was tested
470 with the Shapiro-Wilk test. Non-normally distributed data are presented as box and whisker plots
471 (grand median of all BC means, lower/upper quartiles, 10-90th percentiles); n.s. *p-value* ≥ 0.05, Mann-
472 Whitney U-test *N*: number of animals, *n*: number of endbulbs of Held.
473
474 Next, we investigated whether eEPSC alteration is caused by a reduction in release probability or
475 altered vesicle pool dynamics. We used high frequency stimulation to assess short-term plasticity,
476 release probability as well as the size and dynamics of the RRP during *quasi* physiological regimes of
477 synaptic transmission. Fifty consecutive stimuli were delivered at 100, 200, and 333 Hz (Fig. 3: in the
478 presence of 1 mM kynurenic acid and 100 μM CTZ; Fig. 3-1 in the absence of both drugs). Different
479 from the prominent short-term depression typical for the endbulb of Held (Oleskevich and Walmsley,
480 2002; Yang and Xu-Friedman, 2008), RIM-BP2 deficient endbulb synapses showed an initial facilitation
481 followed by slower depression (Fig. 3, Table 2, Fig. 3-1). Facilitation was evident from the paired pulse
482 ratio (PPR) > 1 in RIM-BP2 deficient endbulb synapses for all inter-stimulus intervals tested, while PPR
483 was consistently ~ 0.8 in WT (Table 2). The extent of depression assessed as EPSC$_{30-50}$/EPSC$_{max}$ (Fig. 3,
484 Table 2, Fig. 3-1) tended to be less in RIM-BP2 deficient endbulb synapses without reaching statistical
485 significance. Release probability (P$_r$) as well as the size and dynamics of the RRP were estimated by
486 applying two variants of the cumulative analysis to the EPSC trains (Fig. 3): Schneggenburger-Meyer-
487 Neher (SMN) method (Schneggenburger et al., 1999) and Elmqvist & Quastel (EQ) method (Elmqvist
488 and Quastel, 1965); for review see: (Neher, 2015). Both methods revealed a significant reduction of
489 P$_r$ in RIM-BP2 KO synapses while RRP size and the replenishment rate were not significantly altered

24

490   (Table 2). In an attempt to address the question whether the reduced release probability reflects a

491   smaller complement of high release probability SVs ("tightly docked" or "super-primed" SVs (Neher

492   and Brose, 2018)) we followed a previously described analysis that found a reduction of SV super-

493   primed SVs upon genetic deletion of all rab3 isoforms (Schlüter et al., 2006). We subtracted the

494   quantal content of each RIM-BP2 KO response from the respective RIM-BP2 WT response during train

495   stimulation (Fig. 3M-O). This analysis revealed the strongest difference between the two genotypes

496   occurs at the beginning of the train, where the RIM-BP2 KO endbulbs release 30-40 SVs less than the

497   RIM-BP2 WT, which is consistent with a reduction of high release probability ("super-primed") SVs in

498   the absence of RIM-BP2. The difference vanishes already after the first two eEPSCs, when the

499   subtraction curves for 200 and 333 Hz actually cross the zero line, indicating that release from KO-

500   synapses is actually slightly larger than that from WT. Possible reasons for this small difference include

501   i) protracted release of low release probability SVs that could result from impaired Ca_V-release site

502   coupling and ii) residual desensitization that is more prominent for RIM-BP2 WT synapses with larger

503   eEPSCs (despite 100 µM cyclothiazide and 1 mM kynurenic acid). During the steady state response to

504   the train stimulation, the WT synapses tended to release more SVs than the KO (average difference:

505   6 SVs for 100 Hz, 3 SVs for 200Hz, no difference for 333 Hz).
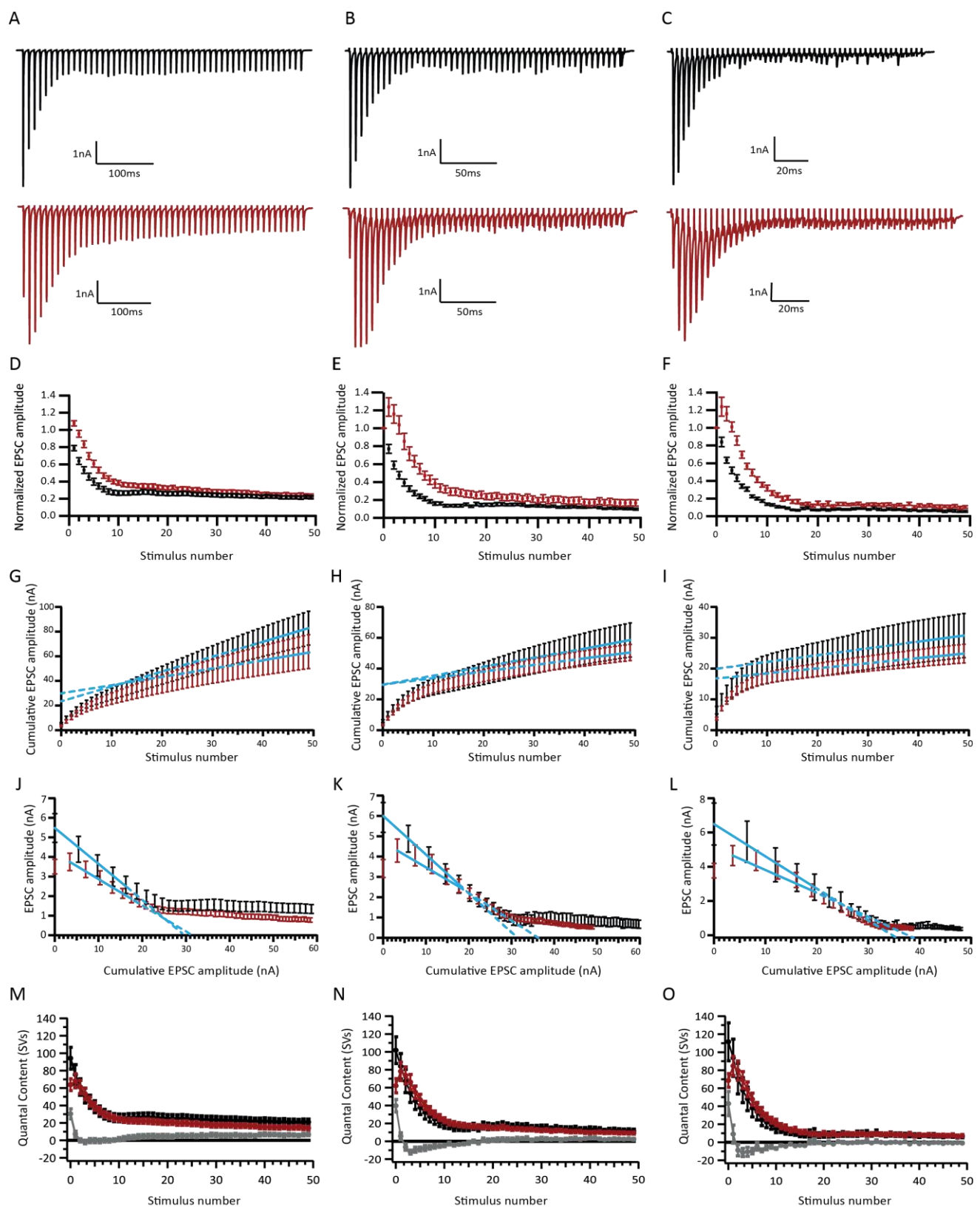
506

507

Figure 3. Analysis of release probability (P_r) as well as the size and dynamics of the RRP

(A-C) Representative traces of eEPSCs in response to trains of 50 action potentials delivered at frequencies of 100 (**A**), 200 (**B**) and 333Hz (**C**) recorded from WT (top, black traces) and RIM-BP2 KO

511 (bottom, red traces). Note the characteristic fast short-term depression of WT bushy cell EPSCs that
512 is altered in the mutant. The mutant BCs show a delayed short-term depression with the first EPSC
513 amplitude not being the largest in the train, indicating that the naive mutant synapse releases most
514 of its vesicles later in the train. (**D, E, F**) Average EPSC amplitudes, normalized to the first EPSC of the
515 train plotted against the stimulus number. (**G-I**) To estimate the size of the readily releasable pool
516 (RRP), the rate of vesicle replenishment and the release probability (P_r) using the Schneggenburger-
517 Meyer-Neher (SMN) method, the EPSC amplitudes of the 100 (**G**), 200 (**H**) and 333Hz (**I**) trains were
518 plotted cumulatively against the stimulus number. The linear fit (solid blue line) to the last ten steady-
519 state values was extrapolated to the y-axis (dotted blue line). The y-intercept value, divided by the
520 average sEPSC amplitude yields the number of vesicles in the RRP. To calculate P_r, the vesicle content
521 of eEPSC1 is divided by the size of the RRP. The slope of the linear fit approximates the rate of vesicle
522 replenishment during the train. Quantitative analysis is further elaborated in Table 1. (**J-L**) To estimate
523 the RRP size and P_r using the Elmqvist and Quastel (EQ) method, absolute EPSC amplitudes were
524 plotted against the cumulative amplitude of all the EPSCs preceding the corresponding EPSC. The
525 linear fit to the first 3-5 points for the 100 (**J**), 200 (**K**) and 333Hz (**L**) trains (solid blue line) was forward
526 extrapolated (dotted blue line) to the x-axis. Dividing the x-axis intercept value by the average sEPSC
527 size, yields the size of the RRP, while the slope of the linear fit defines the P_r. To assess whether the
528 reduced P_r results from fewer "super-primed" SVs in the RRP, a subtraction analysis was performed.
529 We first divided the average eEPSC amplitudes by the average sEPSC amplitude to calculate the SV
530 number released during each eEPSC (quantal content) of the averaged responses to 100, 200 and 333
531 Hz train stimulation. Traces plot the quantal content released during each one of 50 eEPSCs in 100
532 (**M**), 200 (**N**) and 333Hz (**O**) trains against the stimulus number. After subtracting the quantal content
533 for each RIM-BP2 KO eEPSC from the respective WT eEPSC, we plot the subtraction curves (gray
534 curves at the bottom of each panel). For 100 Hz: RIM-BP2 WT N = 14; n = 16, RIM-BP2 KO N = 17; n =
535 21. For 200 Hz: RIM-BP2 WT N = 13; n = 16, RIM-BP2 KO N = 13; n = 16. For 333 Hz: RIM-BP2 WT N =
536 6; n = 12, RIM-BP2 KO N = 14; n = 17. N, number of animals; n, number of BCs.
537

Stimulation Frequency	Parameter	RBP2 WT	RBP2 KO	p value
100Hz	eEPSC1 amplitude (nA)	5.48 ± 0.73 (4.7)	3.5 ± 0.37 (3.6)	**0.022, M**
	tau (ms)	33.60 ± 3.64 (27.2)	56.95 ± 3.76 (58.03)	**0.0001, T**
	$eEPSC_{30-50}$ (nA)	1.29 ± 0.22 (1.09)	0.87 ± 0.12 (0.84)	0.1015, M
	$eEPSC_{30-50}$/EPSCmax	0.23± 0.02 (0.21)	0.24 ± 0.03 (0.24)	0.8205, T
	Replenishment	2.09 ± 0.35 (1.79)	1.44 ± 0.20 (1.2)	0.1015, T
	RRP_{SMN} (SVs)	398.60 ± 72.50 (341.56)	455.61 ± 63.00 (446.32)	0.4038, M
	RRP_{EQ}(SVs)	575.11 ± 102.11 (504.25)	593.62 ± 73.45 (610.12)	0.6826, M
	$P_{r\ SMN}$	0.26 ± 0.02 (0.28)	0.17 ± 0.01 (0.15)	**0.0004, T**
	$P_{r\ EQ}$	0.2 ± 0.02 (0.21)	0.14 ± 0.01 (0.13)	**0.0336, T**
	PPR	0.79 ± 0.03 (0.72)	1.08 ± 0.10 (0.97)	**0.0004, M**
200Hz	tau (ms)	33.05 ± 3.04 (32.46)	70.51 ± 5.85 (65.43)	**<0.0001, M**
	eEPSC30-50 (nA)	0.76± 0.13 (0.70)	0.59 ± 0.07 (0.56)	0.0608, M
	$eEPSC_{30-50}$/EPSCmax	0.13 ± 0.01 (0.14)	0.17 ± 0.03 (0.13)	0.0608, M
	Replenishment	2.16 ± 0.37 (1.98)	1.53 ± 0.24 (1.45)	0.1756,T

27

	RRP_{SMN} (SVs)	479.11 ± 110.23 (351.27)	544.42 ± 77.85 (545.76)	0.3168, M
	RRP_{EQ} (SVs)	554.34 ± 123.03 (441.21)	771.93 ± 108 (663.17)	0.0883, M
	$P_{r\,SMN}$	0.25 ± 0.02 (0.26)	0.14 ± 0.01 (0.13)	**<0.0001, M**
	$P_{r\,EQ}$	0.22 ± 0.02 (0.20)	0.13 ± 0.01 (0.13)	**0.0002, T**
	PPR	0.81 ± 0.05 (0.79)	1.28 ± 0.10 (1.21)	**<0.0001, M**
333Hz	tau (ms)	19.34 ± 2.50 (19.77)	39.97 ± 3.92 (40.97)	**0.0002, T**
	$eEPSC_{30-50}$ (nA)	0.45 ± 0.09 (0.38)	0.48 ±0.08 (0.41)	0.1523, M
	$eEPSC_{30-50}$/EPSCmax	0.07 ± 0.01 (0.07)	0.10 ± 0.02 (0.08)	0.6106, M
	Replenishment	1.24 ± 0.21 (1.22)	1 ± 0.25 (0.89)	0.1656, M
	RRP_{SMN} (SVs)	345.21 ± 96.42 (253.09)	306.16 ± 36.91 (331.58)	0.6471, M
	RRP_{EQ} (SVs)	595.52 ± 155.74 (450.19)	674.17 ± 76.94 (787.59)	0.2635, M
	$P_{r\,SMN}$	0.44 ± 0.06 (0.39)	0.25 ± 0.03 (0.22)	**0.0043, T**
	$P_{r\,EQ}$	0.23 ± 0.03 (0.21)	0.15 ± 0.01 (0.15)	**0.0022, T**
	PPR	0.8 ± 0.05 (0.84)	1.28 ± 0.11 (1.21)	**0.0009, T**

Table 2. Analysis of release probability (P_r) as well as the size and dynamics of the RRP

Tau (τ): time constant of single exponential fit to the decay of eEPSC amplitudes during the stimulation train. **$eEPSC_{30-50}$/EPSCmax**: average amplitude of the last 20 EPSCs (30-50) in the train, normalized to the amplitude of the largest EPSC amplitude of the train. **Replenishment**: rate of vesicle replenishment. **RRP**: readily releasable pool. **P_r**: release probability. **PPR**: paired pulse ratio, amplitude of the second EPSC of the train normalized to the amplitude of the first EPSC. Data are presented as mean ± SEM and medians are shown in parentheses. Normality of data distribution was tested with Jarque-Bera test and the variances were compared with F-test. Statistical significance of differences was assessed with unpaired Student's t-test (shown in the table as T), when the data satisfied the criteria of normality and variance comparability. When the data did not satisfy these criteria, Mann-Whitney U-test was used instead (shown in the table as M). *p-value* < 0.05, set as threshold for statistical significance shown in bold.
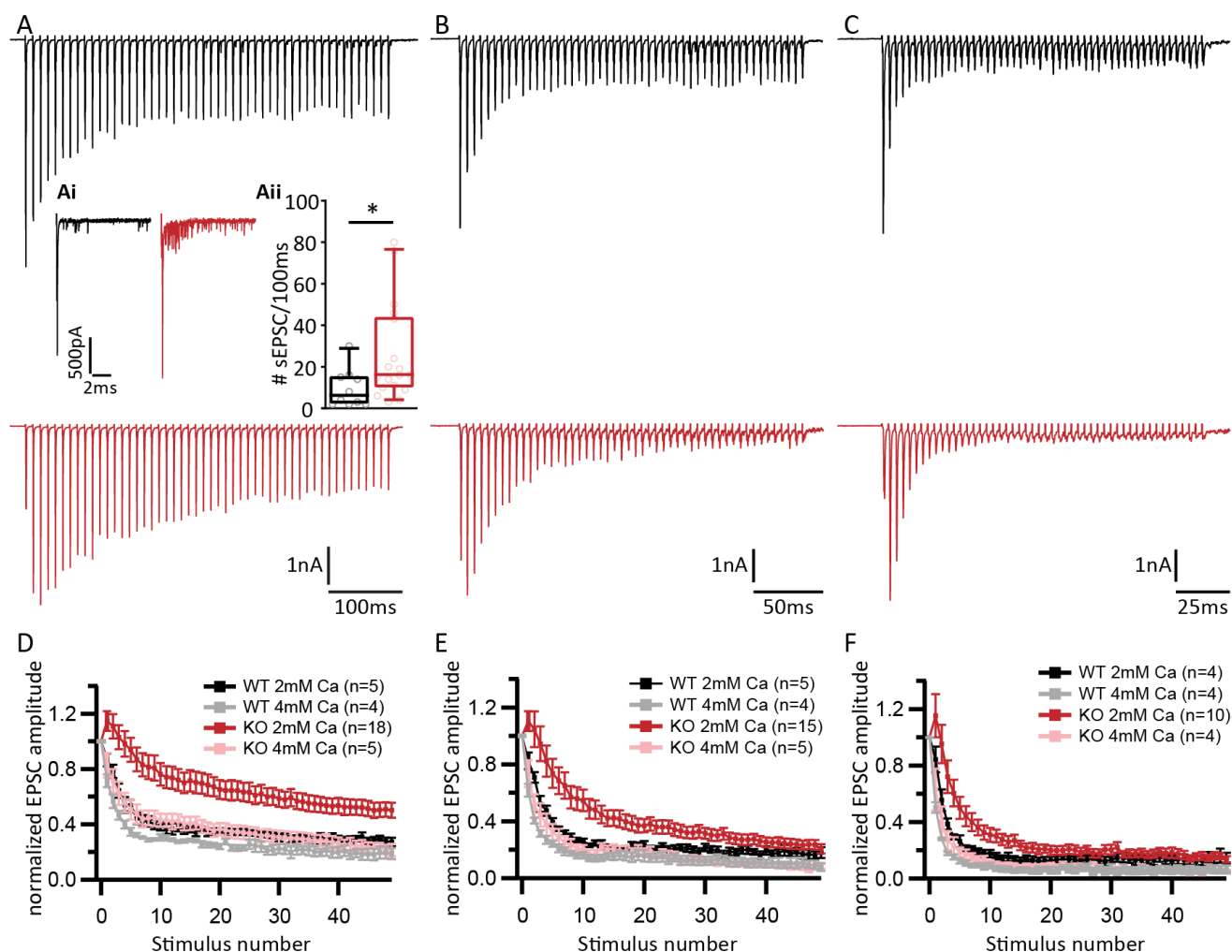
Figure 3-1: Short-term depression replaced by facilitation at endbulbs of Held in RIM-BP2 KO mice in the absence of kynurenic acid and CTZ

Representative traces of eEPSCs in response to trains of 50 action potentials delivered at frequencies of 100 (**A**), 200 (**B**) and 333Hz (**C**) recorded from WT (top, black traces) and RIM-BP2 KO (bottom, red traces). *Inset* (**Ai, Aii**): Asynchronous release calculated as the number of spontaneous EPSC events (sEPSC) within 100 ms following the synchronous release elicited by a train of 50 pulses delivered at 100Hz. A significantly higher asynchronous release was observed in the RIM-BP2 KO (red) as compared to the WT (black). Note the characteristic fast short-term depression of WT bushy cell EPSCs that is altered in the mutant. The mutant BCs show a delayed short-term depression with the first EPSC amplitude not being the largest in the train, indicating that the naive mutant synapse releases most of its vesicles later in the train. This effect is more pronounced in the higher frequencies of stimulation, as is demonstrated when the EPSC amplitudes, normalized to the first EPSC of the train are plotted against the stimulus number (**D, E, F**). This effect was abolished when extracellular Ca^{2+} was increased to 4mM (WT traces in gray and KO traces in pink).

568　In order to further scrutinize RRP dynamics, we studied the recovery from short-term depression, by

569　measuring eEPSC amplitudes elicited by single stimuli presented at varying time intervals after a

570　conditioning 100 Hz train of 50 pulses (Fig. 4). Recovery is displayed as the eEPSC amplitudes

571　normalized to the amplitude of the first eEPSC of the conditioning train (Fig. 4A-B): RIM-BP2 deficient

572　endbulb synapses showed a major reduction of fast recovery. The time course was fitted with a

573　double exponential function revealing the following amplitude and tau values for the fast and slow

574　components of recovery: $A_1 = 0.17 \pm 0.05$, $\tau_1 = 123 \pm 97.6$ ms; $A_2 = 0.69 \pm 0.06$, $\tau_2 = 6.1 \pm 1.7$ s for RIM-

575　BP2 KO and $A_1 = 0.31 \pm 0.04$, $\tau_1 = 96 \pm 30$ ms; $A_2 = 0.4 \pm 0.04$, $\tau_2 = 4.6 \pm 1.4$ s for WT.

576　　　Next, we evaluated the impact of the impaired synaptic transmission on processing of

577　auditory information using juxtacelluar recordings from putative spherical bushy cells (for simplicity

578　refered to as "BCs") *in vivo* (Fig. 5). Glass microelectrodes were stereotactically navigated to the aVCN

579　from an occipital craniotomy, sound stimuli were presented in the open field, and BCs identified

580　based on electrode position, first spike latency, regularity of firing and shape of the peristimulus spike

581　time histogram (see Materials and Methods). The (non-significant) trend toward lower spontaneous

582　firing rate (Fig. 5A, Table 3) is consistent with the reduced spontaneous ANF input (Krinner et al.,

583　2017) and the trend toward a lower frequency of sEPSCs in RIM-BP2 KO BCs (Fig. 1-2). Sound

584　threshold and frequency tuning were unaltered, whereby the RIM-BP2 KO data set contained more

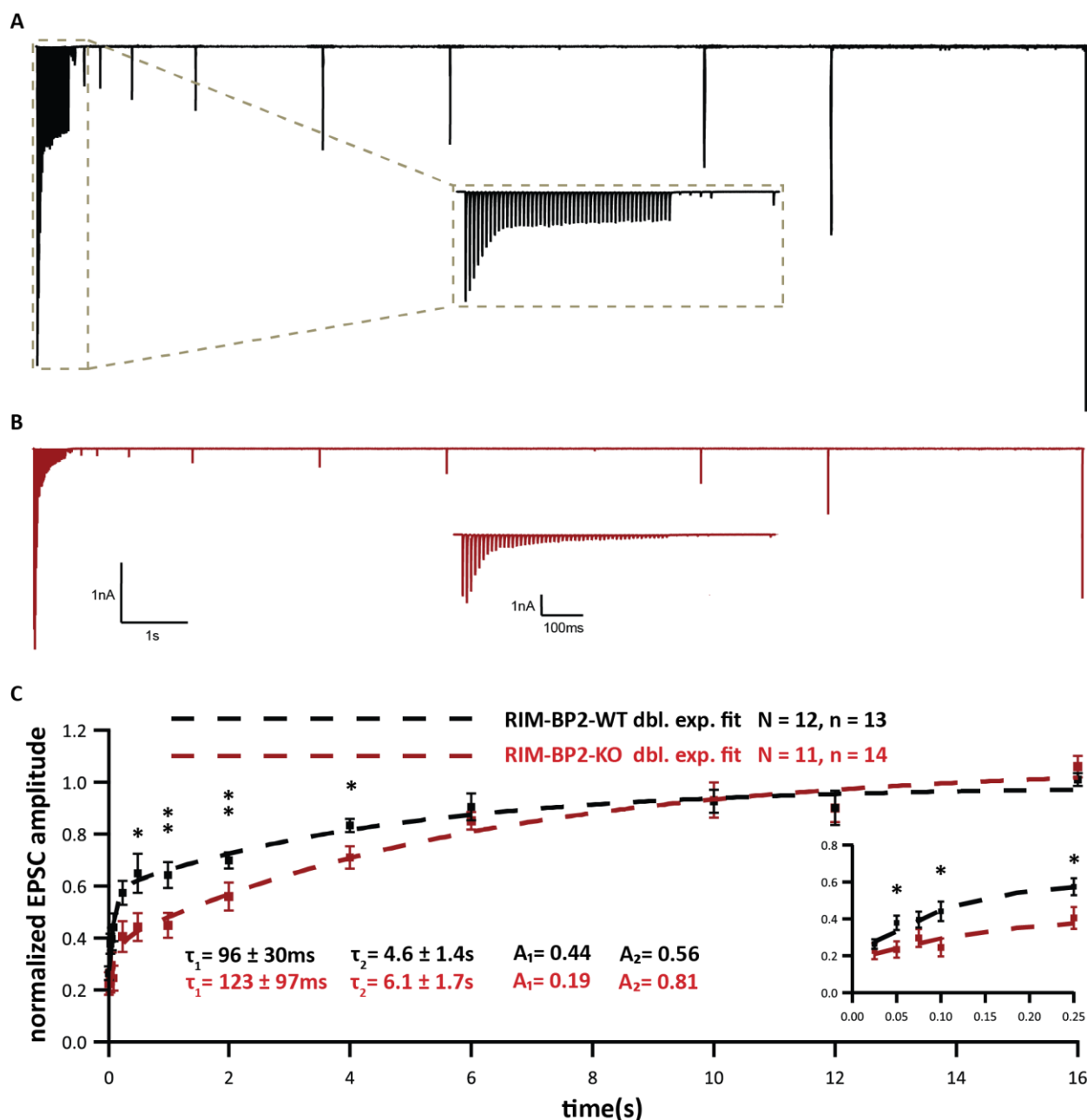585　BCs with higher characteristic frequency (Fig. 5B-C, Table 3).

Figure 4. Slowed RRP recovery in RIM-BP2 deficient endbulb synapses.
(A-B) Representative traces of RIM-BP2 WT (**A**) and RIM-BP2 KO (**B**), illustrate the recovery experiment. After a 100 Hz conditioning train of 50 stimuli, single test pulses were delivered at time intervals of (in ms) 25, 50, 75, 100, 250, 500 (further intervals in s), 1, 2, 4, 6, 10, 12 and 16. To assess recovery, the EPSC amplitude in response to the test pulse is normalised to the first EPSC amplitude of the conditioning train. Insets (**A, B**) show the time course of recovery during the first 5 test stimuli in sub-second detail. (**C**) Recovery is plotted as mean ± SEM EPSC amplitude in response to test pulses normalized to the first EPSC amplitude of the conditioning train. The double exponential fits are represented by the dashed lines for RIM-BP2 WT (black) and RIM-BP2-KO (red). The time constants (τ) and fractional contributions (A) of fast (τ_1, A_1) and slow (τ_2, A_2) recovery components are provided on the graph. Inset shows the first five responses in detail. Normality was tested with Jarque-Bera test. Statistical significance between groups was tested with Mann-Whitney U-test. **$p\text{-}value < 0.01$, *$p\text{-}value < 0.05$. N: number of animals, n: number of BCs

600   The peak firing rate at sound onset was significantly reduced in RIM-BP2 KO BCs (Fig. 5D, by

601   approximately 40%, Table 3) compatible with the reduced initial release probability. The adapted

602   firing rates were not significantly reduced (Fig. 5Dii, Table 3), which is consistent the better

603   maintained EPSC amplitudes during steady state response to train stimulation in BCs (RIM-BP2 WT:

604   1.2 ± 0.2 nA, RIM-BP2 KO: 0.9 ± 0.1) (Fig. 3A-F, Table 2) and the normal adapted firing rate of ANFs

605   (Krinner et al., 2017) .

606   In addition, we found the temporal jitter of the first spike after stimulus onset to be greater in

607   RIM-BP2 KO BCs, while the first spike latency was comparable between the two genotypes (Fig. 5E,

608   Table 3). The stronger reduction of the peak rate and increased first spike latency jitter of BCs in

609   comparison to ANF likely reflects the impaired transmission at the RIM-BP2-deficient endbulb, which

610   degrades information processing in the lower auditory pathway beyond what is caused by the mildly

611   affected synaptic sound encoding in the cochlea. This hypothesis is further supported by the auditory

612   brainstem responses of RIM-BP2 KO mice, which show a more pronounced amplitude decline for the

613   aVCN related wave III than for the auditory nerve related wave I (Krinner et al., 2017)). In conclusion,

614   the reduced release probability of the endbulbs impairs the transmission of sound onset information,

615   which is likely to hamper hearing and auditory tasks such as gap detection and sound localization in
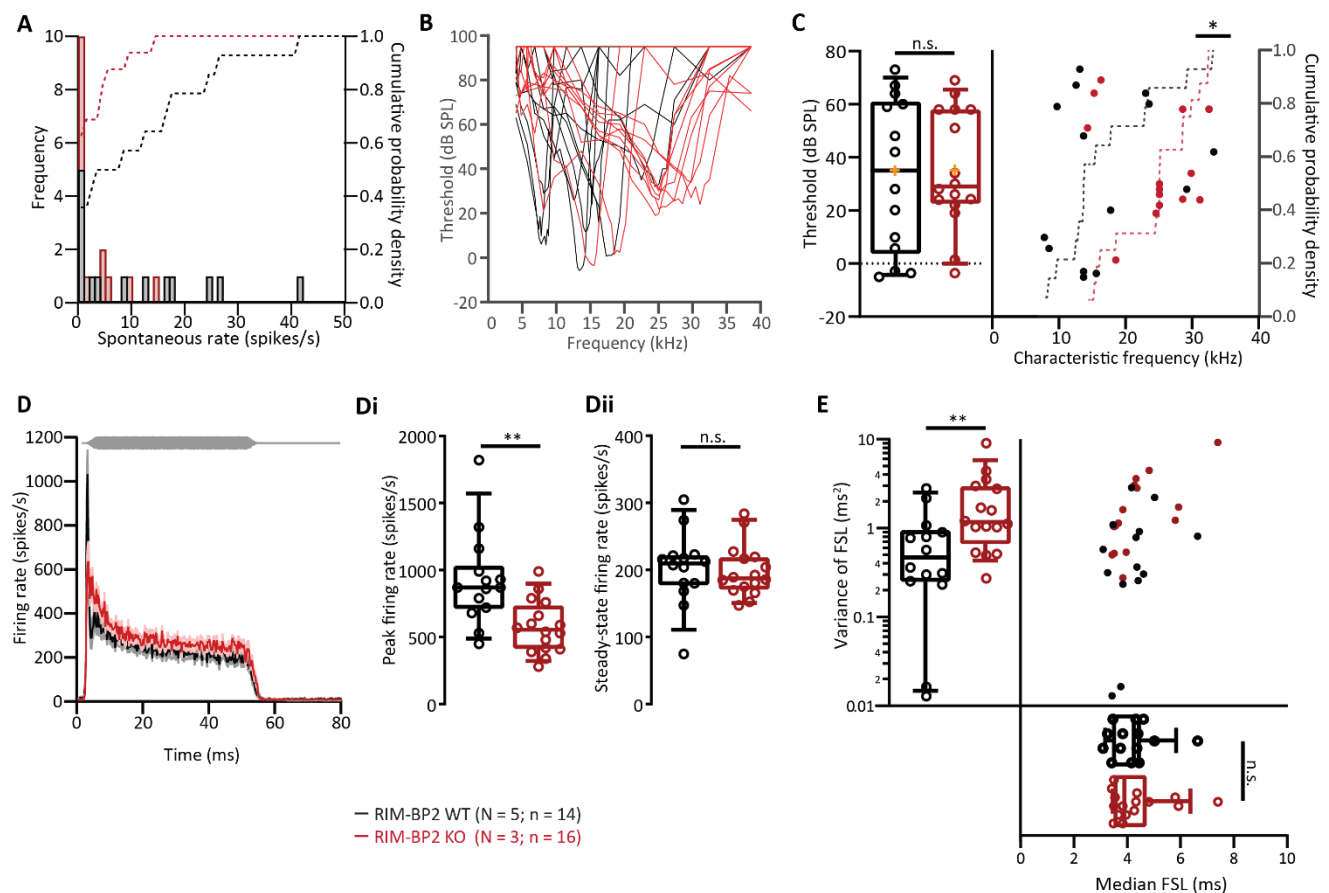
616   particular.

617

618

Figure 5. Impaired transmission of sound information in aVCN of RIM-BP2 KO mice *in vivo*.
(**A**) Comparable distribution of spontaneous firing rates of single BCs in RIM-BP2 WT (black) and RIM-BP2 KO (red). The histogram represents the distribution of their frequency (left y-axis) and the dotted lines represent the cumulative probability density (right y-axis) of spontaneous firing rates. (**B-C**) Representative tuning curves of BC from RIM-BP2 WT (black) and RIM-BP2 KO (red) demonstrate preserved sharp frequency tuning and low thresholds at the characteristic frequencies (frequency for which spike rate increase requires least sound intensity, **C,** *left*) in RIM-BP2 KO BCs. For unknown reasons, we encountered more BCs with high characteristic frequency in RIM-BP2 KO (**C,** *right*). (**D**) Rise-aligned peristimulus time histogram (PSTH) of the BC response to 50 ms tone burst stimulation (at characteristic/best frequency, 30 dB above threshold, stimulus represented in gray) in RIM-BP2 WT (black; N=5; n=14) and RIM-BP2 KO (red; N=3; n=16). PSTH presented as mean (solid lines) ± SEM (shaded area). Peak onset firing rate was significantly reduced in RIM-BP2 KO BCs (**Di**) while the steady-state firing rate was comparable between the two genotypes (**Dii**). Variance in the first spike latency of PSTH (in D) was increased in RIM-BP2 KO units while the median first spike latency remained unperturbed (**E**). Data information: Significance levels: n.s. $p \geq 0.05$, *$p < 0.05$, **$p < 0.01$; n = number of BCs and N = number of mice. Box and whisker plot represents median, lower/upper quartiles and 10-90th percentiles. Each data point represents the response of a BC. For details about mean ± SEM, median, sample size and statistics see Table 3.

33

| Parameter	RIM-BP2 WT (N = 5; n = 14)	RIM-BP2 KO (N =3; n = 16)	p value
Spontaneous rate (spikes/s)	10.90 ± 3.42 (5.88)	2.74 ± 1.07 (0.60)	0.18, M
Threshold (dB SPL)	33.20 ± 7.76 (35.00)	35.20 ± 5.50 (29.00)	0.83, T
Characteristic frequency (kHz)	16.75 ± 2.06 (13.66)	24.21 ± 1.59 (25.05)	**0.015, K**
Peak firing rate (spikes/s)	922.10 ± 91.65 (870.00)	575.60 ± 49.24 (555.00)	**0.0033, TW**
Steady-state firing rate (spikes/s)	202.30 ± 14.53 (209.80)	197.80 ± 9.6 (187.40)	0.79, T
Variance of FSL (ms^2)	0.76 ± 0.22 (0.47)	2.11 ± 0.56 (1.18)	**0.008, M**
Median FSL (ms)	4.20 ± 0.24 (4.25)	4.36 ± 0.28 (3.90)	0.93, M

637 **Table 3. Analysis of *in vivo* extracellular recordings from single BCs**
638 Data are presented as mean ± SEM and medians are shown in parentheses. Normality of data
639 distribution was tested with Kolmogorov-Smirnov test and the variances were compared with F-test.
640 Statistical test used to assess the significance of differences is indicated in the column of p-value.
641 Unpaired Student's t-test (shown in the table as T) was used, when the data satisfied the criteria of
642 normality and variance comparability. Normally distributed data with unequal variances were
643 compared using Student's t-test with Welch's correction (shown in the table as TW). Non-normally
644 distributed data were tested with Mann-Whitney U-test or Kolmogorov-Smirnov test (shown in the
645 table as M and K respectively). *p-value* < 0.05, set as threshold for statistical significance shown in
646 bold.

647

648 **RIM-BP2 disruption appears not to alter the molecular composition of the endbulb active zones**

649 Given the scope of protein interactions of RIM-BP that includes Ca^{2+} channels, large conductance Ca^{2+}

650 activated K^+ channels (Sclip et al., 2018) and multi-domain proteins of the AZ, we considered the

651 possibility that some of the above described physiological alterations might reflect changes in the

652 abundance of other AZ proteins. In order to test for potential effects of RIM-BP2 disruption on the

653 molecular composition of the AZs, we performed semi-quantitative, confocal immunofluorescence

654 microscopy in coronal brain slices. RIM-BP2 WT and RIM-BP2 KO samples were harvested and

655 processed strictly in parallel. Likewise, images were acquired using the same laser power and gain

656 settings at the same confocal microscope. Excitatory AZs facing the postsynaptic BC were identified

657 by co-localization of immunofluorescence of the targeted AZ protein with the immunofluorescence

658 of the vesicular glutamate transporter VGlut1 or a juxtaposition to the immunofluorescence of homer

659 1, a scaffold of excitatory synapses and a lack of juxtaposition to immunofluorescence of gephyrin, a

34

660   scaffold of inhibitory synapses (Fig. 6). We focused our analysis on the spherical or ovoid BC soma

661   which are engaged by a corona of synapses. Staining for RIM-BP2 showed the expected corona of

662   immunofluorescence spots in WT slices, but no obvious synaptic immunofluorescence in RIM-BP2 KO

663   slices (Fig. 6A, Fig. 6B, left: integrated fluorescence within the Vglut1 positive volume, right: lack of

664   spots). We did not observe significant differences in the integrated immunofluorescence or the

665   number of puncta of Munc13-1 (Fig. 6C, D), RIM2 (Fig. 6E, F), CAST (Fig. 6G, H), and bassoon (Fig. 6I,

666   J) in RIM-BP2 KO slices, suggesting an unaltered abundance of these multi-domain proteins at the

667   excitatory AZ facing the BC in the absence of RIM-BP2.
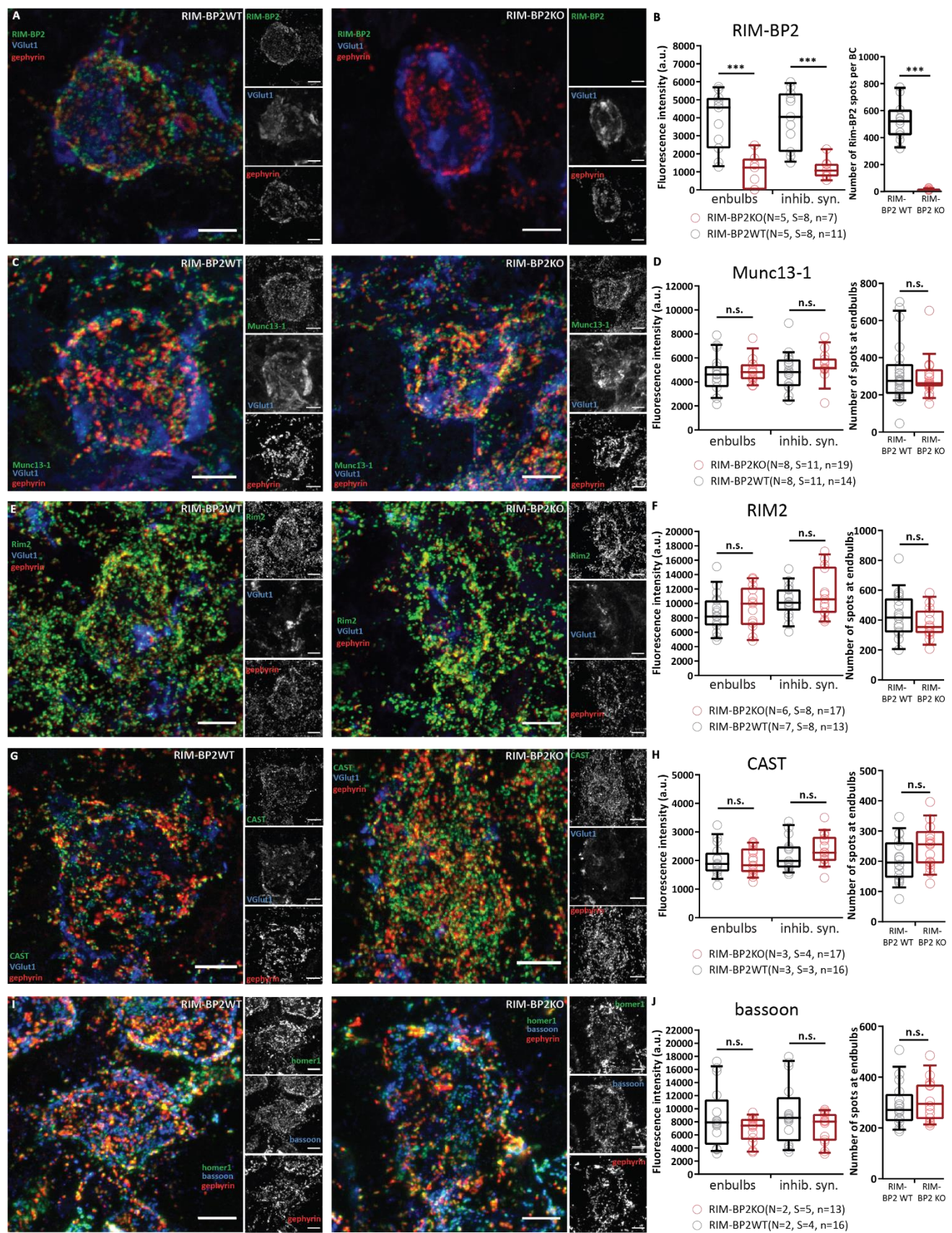
670 **Figure 6. RIM-BP2 disruption does not seem to alter the molecular composition of the endbulb**
671 **active zones**
672 (**A, C, E, G, I**) Representative maximal z-projections of confocal image stacks of BCs in RIM-BP2 WT
673 shown on left and RIM-BP2 KO on right. 30 μm coronal brainstem slices were immunolabelled for
674 RIM-BP2 (**A**), Munc13-1 (**C**), RIM2 (**E**) and CAST (**G**) and co-stained for VGlut1 to outline endbulbs and
675 gephyrin for inhibitory synapse labelling. For bassoon immunolabelling (**I**) we co-stained for homer1
676 (excitatory postsynapses) and gephyrin. (**B, D, F, H, J**) Quantification of fluorescence intensity of CAZ
677 proteins at endbulbs and inhibitory synapses of BCs (*left*), and the number of spots of the targets CAZ
678 protein at endbulbs (*right*). (**A**) Representative z-projection shows loss of RIM-BP2 immunoreactivity
679 in the RIM-BP2 KO brainstem sliced. There was only a faint residual and likely unspecific signal
680 remaining at excitatory and inhibitory synapses (**B**, left), RIM-BP2 immunofluorescent spots were
681 nearly abolished (**B**, right). The immunofluorescence intensity of Munc13-1 (**D**), RIM2 (**F**), CAST (**H**)
682 and bassoon (**J**) were unaltered at RIM-BP2 KO endbulbs. Right columns of D, F, H, J show similar
683 number of CAZ protein spots localized at KO endbulb AZs as in the WT AZs. The numbers were
684 calculated by subtracting the gephyrin colocalized spots from the total number of spots per BC. The
685 data are presented as box and whiskers plots (grand median of mean estimates for all BCs,
686 lower/upper quartiles, 10-90th percentiles). Each data point represents the mean estimate of
687 fluorescence intensity of the active zones of each BC included in the analysis. Statistical significance
688 of differences between groups was determined with unpaired Student's t-test (with Welch's
689 correction, when variances differed significantly), if the data's distribution did not differ from a
690 normal distribution or with Mann-Whitney U test in case of non-normally distributed data. Normality
691 of distribution was tested with Jarque-Bera test and variances were compared with F-test. n.s. p-
692 value ≥ 0.05. Samples from RIM-BP2 WT and RIM-BP2 KO mice, aged p15-p21 were harvested and
693 processed strictly in parallel and images were acquired in parallel using the same laser power and
694 gain settings at the same confocal microscope. Data information: *N*: number of animals, *S*: number
695 of slices, *n*: number of BCs. All scale bars: 5μm
696
697 **Increased Ca^{2+} influx improves release probability but unmasks impaired SV replenishment during**

698 **train stimulation**

699 Unaltered Ca^{2+} influx and RRP size but reduced P_r led us to focus the analysis on the coupling of Ca^{2+}

700 channels to SV release. As a first approach we increased the presynaptic Ca^{2+} influx by elevating the

701 extracellular Ca^{2+} concentration $[Ca^{2+}]_e$ from physiological (2mM) to 4mM. This manipulation

702 abolished the differences in P_r (both time course of depression and PPR were WT-like, Fig. 7, Table

703 4). This is consistent with a greater diffusional distance between Ca^{2+} channels and SV release sites

704 that can be overcome when more Ca^{2+} enters per channel opening. Alternatively, or in addition,

705 greater Ca^{2+} influx might foster Ca^{2+} dependent priming or facilitation of release. In addition,

37

706   increased Ca^{2+} influx unmasked a slowed SV replenishment during train stimulation in RIM-BP2

707   deficient endbulbs.
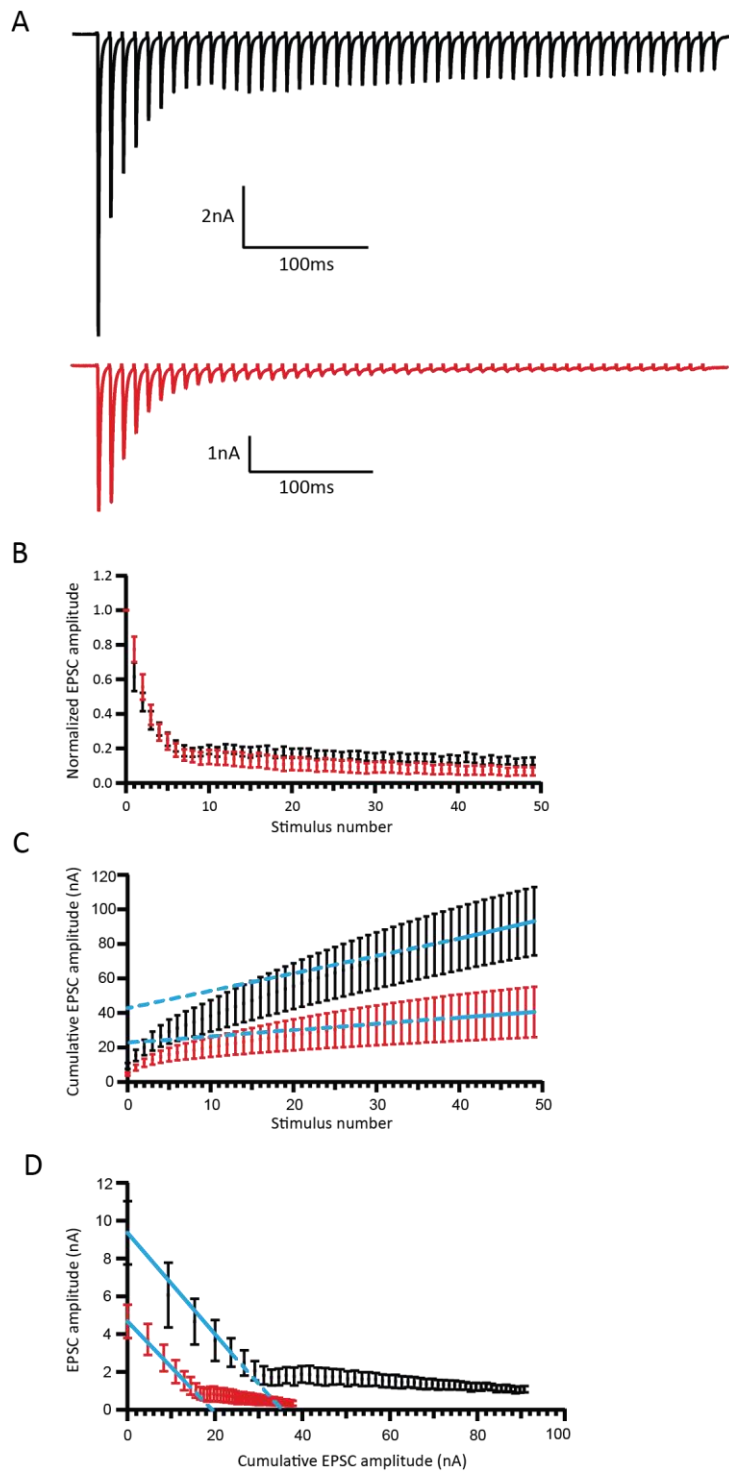
708
709   **Figure 7. Analysis of release probability (P_r) as well as the size and dynamics of the RRP at 4 mM**
710   **$[Ca^{2+}]_e$**
711   (**A**) Representative traces of eEPSCs in response to trains of 50 action potentials delivered at a 100 Hz
712   frequency, recorded from WT (top, black traces) and RIM-BP2 KO (bottom, red traces). When the

713 mutant terminals are exposed to 4mM $[Ca^{2+}]_e$, a WT-like depression pattern is restored. (**B**) This is
714 even more obvious when the mean EPSC amplitudes, normalized to the first EPSC of the train are
715 plotted against the stimulus number. (**C**) We estimate the size of the readily releasable pool (RRP),
716 the rate of vesicle replenishment during the train and the release probability (P_r) using the SMN
717 method. (**D**) We estimate the RRP size and P_r using the Elmqvist and Quastel (EQ) method. For 100
718 Hz: RIM-BP2 WT N = 7; n = 7, RIM-BP2 KO N = 5; n = 5. N, number of animals; n, number of BCs.
719 Quantitative analysis is further elaborated in Table 4.
720

Stimulation Frequency	Parameter	RBP2 WT	RBP2 KO	p value
100Hz	eEPSC1 amplitude (nA)	9.36 ± 1.67 (8.07)	4.67 ± 0.88 (4.05)	**0.035, T**
	tau (ms)	21.76 ± 3.44 (20.17)	29.19 ± 4.50 (32.89)	0.2115, T
	eEPSC$_{30\text{-}50}$	1.22 ± 0.21 (1.23)	0.41 ± 0.18 (0.46)	0.2020, M
	eEPSC$_{30\text{-}50}$/EPSCmax	0.14 ± 0.02 (0.13)	0.08 ± 0.03 (0.10)	0.1125, T
	Replenishment	1.91 ± 0.29 (1.96)	0.66 ± 0.26 (0.78)	**0.0116, T**
	RRP$_{SMN}$ (SVs)	666.43 ± 219.15 (363.98)	415.15 ± 155.94 (331.33)	0.5303, M
	RRP$_{EQ}$(SVs)	602.61 ± 168.87 (518.41)	358.88 ± 102.66 (320.26)	0.3434, M
	$P_{r\,SMN}$	0.31 ± 0.04 (0.27)	0.26 ± 0.04 (0.22)	0.4168, T
	$P_{r\,EQ}$	0.30 ± 0.04 (0.30)	0.27 ± 0.04 (0.24)	0.6034, T
	PPR	0.62 ± 0.08 (0.63)	0.77 ± 0.07 (0.79)	0.2677, M

721
722 **Table 4. Analysis of release probability (P_r) as well as the size and dynamics of the RRP at 4 mM**
723 **$[Ca^{2+}]_e$**
724 **Tau (τ)**: time constant of single exponential fit to the decay of eEPSC amplitudes during the
725 stimulation train. **eEPSC$_{30\text{-}50}$/EPSCmax**: average amplitude of the last 20 EPSCs (30-50) in the train,
726 normalized to the amplitude of the largest EPSC of the train. **Replenishment**: rate of vesicle
727 replenishment during the train. **RRP**: readily releasable pool. **P_r**: release probability. **PPR**: paired pulse
728 ratio, amplitude of the second EPSC of the train normalized to the amplitude of the first EPSC. Data
729 are presented as mean ± SEM and medians are shown in parentheses. Normality of data distribution
730 was tested with Jarque-Bera test and the variances were compared with F-test. Statistical significance
731 of differences was assessed with unpaired Student's t-test (shown in the table as T), when the data
732 satisfied the criteria of normality and variance comparability. When the data did not satisfy these
733 criteria, the Mann-Whitney U-test was used instead (shown in the table as M). *p-value* < 0.05, set as
734 threshold for statistical significance shown in bold.
735
736

737 **RIM-BP2 disruption alters the topography of Ca²⁺ channels at endbulb active zones**

738 In order to probe for potential morphological correlates of altered release probability we employed

739 immunofluorescence microscopy and electron microscopy of immunolabeled Ca²⁺ channels. First, we

740 performed a strictly parallel study of $Ca_V2.1$ distribution at excitatory synapses around the BCs of

741 RIM-BP2 KO and WT mice using stimulated emission depletion (STED) nanoscopy (Fig. 8A-K) as well

742 as confocal microscopy (as described above, Fig. 8-1A, B). We used bassoon and homer1 as context

743 markers to analyse the presynaptic $Ca_V2.1$ immunofluorescence distribution. Both the integrated

744 $Ca_V2.1$ immunofluorescence intensity per AZ and the number of $Ca_V2.1$ puncta were unaltered at the

745 confocal level (Fig. 8-1B), which is consistent with finding normal presynaptic Ca²⁺ influx (Fig. 2). For

746 our 2-colour STED analysis we focused on AZ/PSD appositions ($Ca_V2.1$/homer1, bassoon/homer1) of
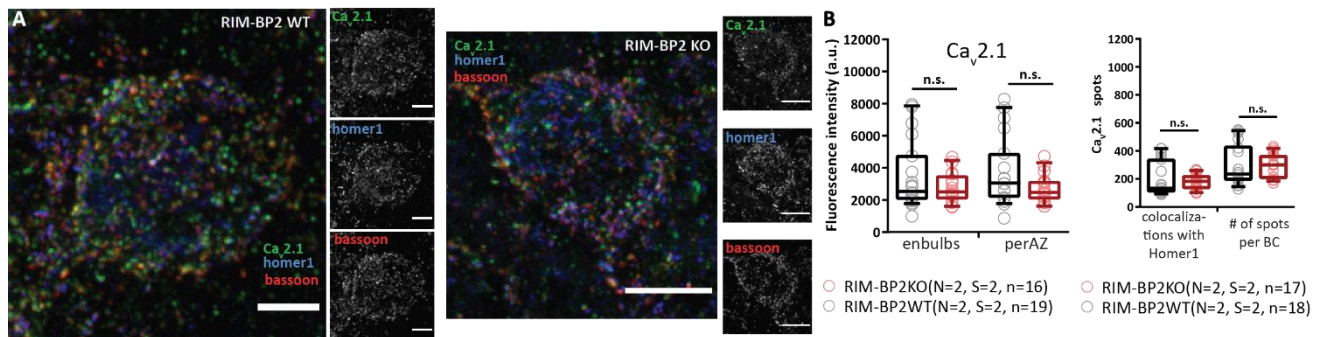
747 endbulbs of Held.

748

749 **Figure 8-1: Unaltered $Ca_V2.1$ immunofluorescence intensity in RIM-BP2-deficient endbulbs of Held**

750 (**A**) Maximal z-projections from confocal image stacks display the immunolabelling against $Ca_V2.1$,
751 bassoon and homer1 at endbulb AZs in coronal brain-stem slices of mouse aVCN. (**B**) No quantitative
752 change was found in the integrated immunofluorescence (*left*) or number (*right*) of $Ca_V2.1$ puncta in
753 either the excitatory endbulb AZs (juxtaposed to homer1 immunofluorescence) or all AZs (endbulb +
754 inhibitory AZ) facing BC of RIM-BP2 KOs. *p-value* < 0.05. *N*: number of animals, *S*: number of slices,
755 *n*: number of BCs.
756
757 We interpret the $Ca_V2.1$ and bassoon puncta discerned by STED to represent individual AZs. As the

758 PSD was studied at confocal resolution, we assume the larger homer1-spots represent a merger of

759 several small PSDs. We operationally defined the organization of several $Ca_V2.1$ or bassoon puncta

760   around a single homer1 spot a synaptic contact assembly (SCA) whereby its center corresponds to

761   the center of the homer1 punctum. Our analysis indicated a wider spatial distribution of $Ca_V2.1$

762   puncta in RIM-BP2 KO which localized further away from the SCA center and from each other (Fig.

763   8A-K), suggestive of a more dispersed $Ca_V2.1$ topography. Similar findings were made for bassoon
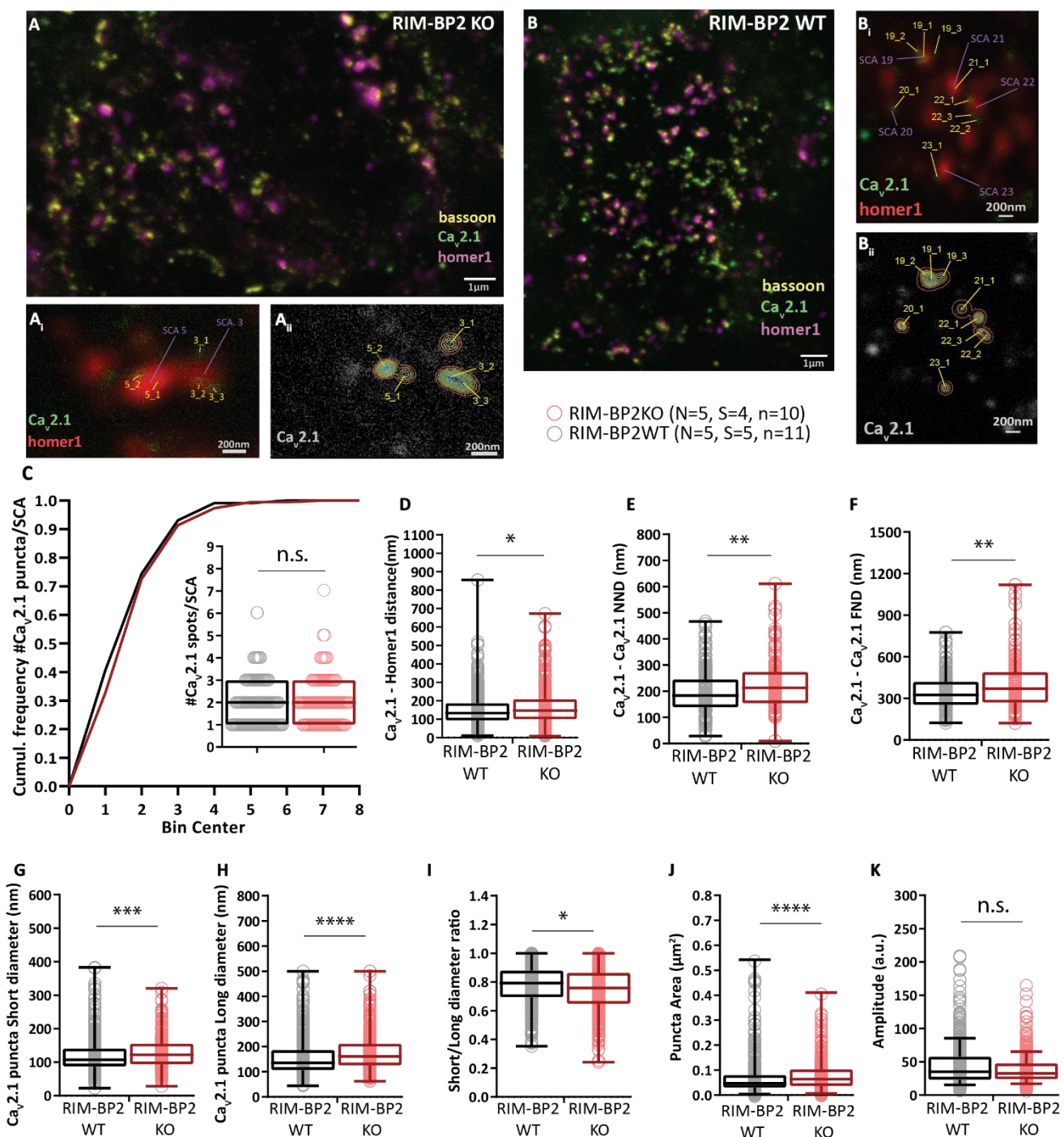
764   (Fig. 8-2).

765

Figure 8 RIM-BP2 disruption alters the topography of Ca²⁺ channels at endbulb active zones

(**A-B**) Analysing sections from 20 μm thick brain slices stained for $Ca_V2.1$ (STED), bassoon (STED) and homer1 (Confocal) with STED nanoscopy, uncovered differences in the topography and dimensions of $Ca_V2.1$ clusters at AZ – to – PSD SCAs of RIM-BP2 WT (**A, A$_i$, A$_{ii}$**) and RIM-BP2 KO (**B, B$_i$, B$_{ii}$**) endbulb terminals. (**C**) The number of clusters per SCA is unchanged in the KO. In the absence of RIM-BP2, the $Ca_V2.1$ puncta (yellow tags **A$_i$, A$_{ii}$, B$_i$, B$_{ii}$**) are located further from the center of the SCA (**D**), defined as the center of the Homer1 puncta (violet tags **A$_i$, B$_i$**). The clusters are also located further apart from each other, shown by increased Nearest Neighbour (**E**) and Furthest Neighbour (**F**) distances within SCAs. (**G, H, J**) 2D – Gaussian fitting yielded the short and long cluster diameters at half maxima. (**I**) The deletion of RIM-BP2 leads to larger and more elongated $Ca_V2.1$ puncta at the endbulb of Held

42

777 active zones. (**K**) The amplitude of fluorescence at the center of Ca$_V$2.1 puncta does not differ
778 significantly between RIM-BP2 WT and RIM-BP2 KO active zones. Normality was tested with Jarque-
779 Bera test. Statistical significance between groups was tested with Mann-Whitney U-test for non-
780 normally distributed data or with Student's t-test. ****$p\text{-value} < 0.0001$, ***$p\text{-value} < 0.001$, **$p\text{-}$
781 $value < 0.01$, *$p\text{-value} < 0.05$. *N*: number of animals, *S*: number of slices, *n*: number of BCs.
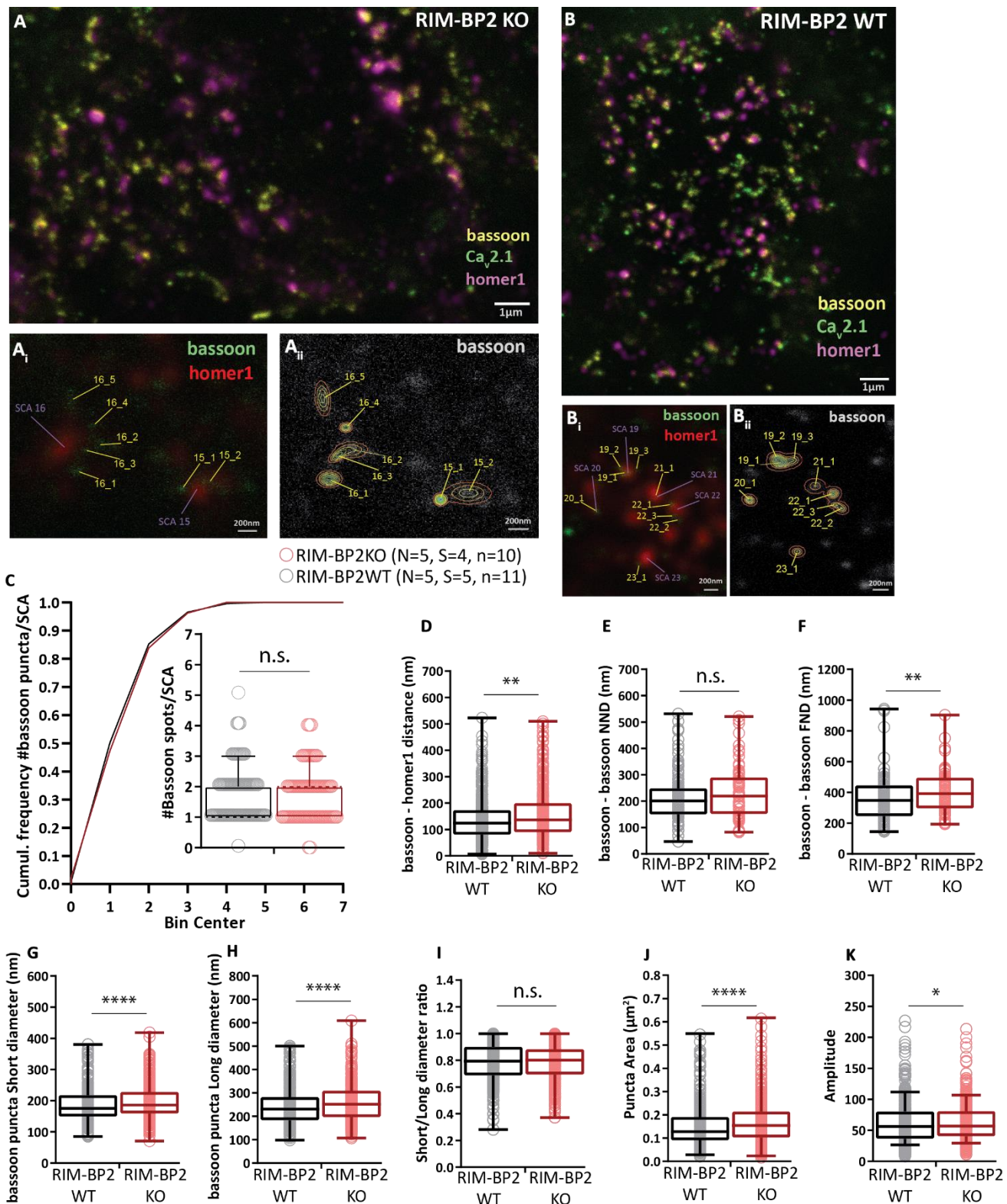782

783

43

784 **Figure 8-2. RIM-BP2 disruption alters distribution and extent of bassoon clusters marking the**
785 **presynaptic density of endbulb active zones**
786 Analysing sections (**A, B**) from 20 μm thick brain slices stained for $Ca_V2.1$ (STED), bassoon (STED) and
787 homer1 (Confocal) with super-resolution STED microscopy, uncovered differences in the amplitude
788 of fluorescence, topography and dimensions of bassoon positive puncta in the absence of RIM-BP2.
789 The bassoon puncta were detected and fitted with 2D – Gaussian functions at AZ – to – PSD SCAs of
790 RIM-BP2 WT (**A, A$_i$, A$_{ii}$**) and RIM-BP2 KO (**B, B$_i$, b$_{ii}$**) endbulb terminals. The number of puncta per SCA
791 is unchanged in the KO (**C**). In the absence of RIM-BP2, the bassoon puncta (yellow tags **A$_i$, A$_{ii}$, B$_i$, B$_{ii}$**)
792 are located further from the center of the SCA (**D**), defined as the center of the postsynaptic homer1
793 puncta (violet tags **A$_i$, B$_i$**). We found no significant difference in the Nearest Neighbour distance (**E**).
794 Furthest neighbour distance (**F**) was significantly increased in the mutant. Comparing the short and
795 long puncta diameters at half maxima, shows that the deletion of RIM-BP2 leads to proportionally
796 (no change in short/long diameter ratio, **I**) larger (**G, H, J**) bassoon puncta at endbulb of Held active
797 zones. The amplitude of fluorescence at the center of bassoon puncta is significantly increased RIM-
798 BP2 KO active zones (**K**). Normality was tested with Jarque-Bera test. Statistical significance between
799 groups was tested with Mann-Whitney U-test for non-normally distributed data and with Student's
800 t-test for data showing a normal distribution. ****p-value < 0.0001, ***p-value < 0.001, **p-value <
801 0.01, *p-value < 0.05. N: number of animals, S: number of slices, n: number of BCs.
802

803 We then turned to immunolabelling of $Ca_V2.1$ in SDS-treated freeze-fracture replica (SDS-FRIL,

804 (Nakamura et al., 2015)). To image the endbulbs onto the BCs, we focused on the BC rich rostral-most

805 aVCN sections of the brainstem. Endbulb terminals were prominently distinguishable in our replicas

806 by their large size synapsing on to the BC soma (Fig. 9-1A). We also validated that we were imaging

807 the correct area and cell type, by analysing the intramembrane particle (IMP) clusters representing

808 PSDs on the exoplasmic face (E-face) of the BC soma (Fig. 9-1C-F). Our estimates of PSD areas (Fig. 9-

809 1B, Table 5) were comparable to the ones previously reported for ANF-BC synapses (Rubio et al.,

810 2017). We then assessed the protoplasmic face (P-face) of the replicas for the analysis of AZ proteins

811 and $Ca_V2.1$ channel distribution (Fig. 9-2). AZs were located by simultaneous immunolabelling of three

812 characteristic AZ proteins: RIM, neurexin, and ELKS with 5 nm gold particles. The number of AZ

813 particles was less than that previously observed in other types of synapses (Miki et al., 2017) which

814 might reflect lower expression of ELKS in the endbulb synapses. Since the samples from both

815 genotypes were handled simultaneously by the same experimenter, the comparison between the

44

816   genotypes remains valid. Nonetheless, given the low labelling efficiency for AZ proteins, we used AZ

817   markers primarily to identify the location of AZs. AZ area was characterized by IMPs of distinct shape,

818   number and size compared with those in surrounding areas, and demarcated manually by connecting

819   the outermost IMPs (Fig. 9-2B-C). The estimated AZ area was comparable between RIM-BP2 KO and

820   WT (Fig. 9-2D). When analysing the distribution of $Ca_V2.1$ channels labelled with 10 nm gold particles

821   within the AZ area, both the number and density of $Ca_V2.1$ particles were significantly reduced in the

822   RIM-BP2 KO (Fig. 9-2G-H, Table 5).

823
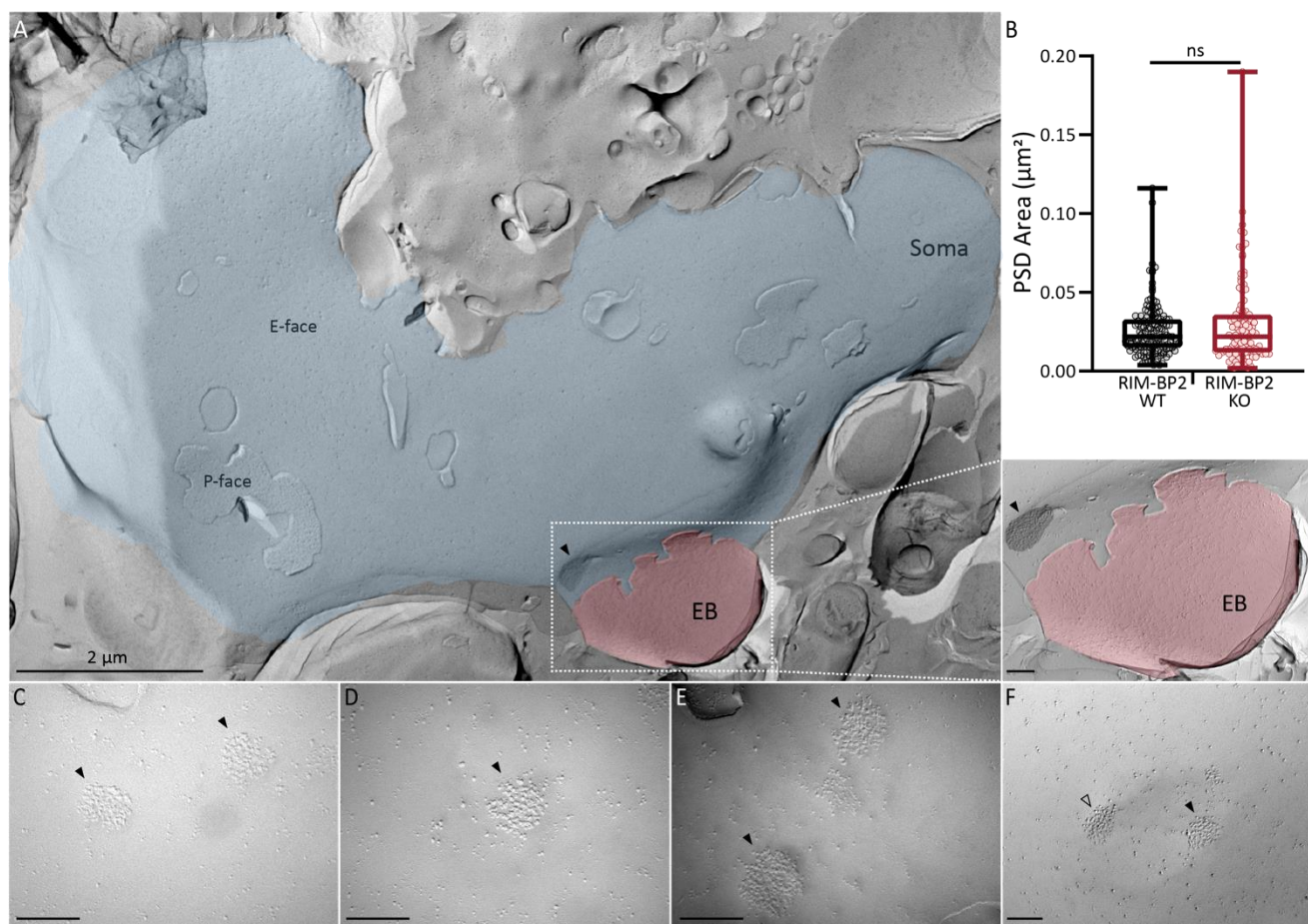
824   **Figure 9-1. Identification of endbulb of Held synapses**

825   (**A**) SDS-FRIL electron micrograph at low magnification (9700x) showing E-face of a bushy cell (BC)
826   soma (blue) with patches of P-face, contacted by an endbulb (red). IMP-cluster representing the PSD
827   of auditory nerve on the BC soma highlighted in black with a solid black arrow head. Inset shows the
828   magnified (97,000x) view of the endbulb synapse on to the BC with a PSD IMP-cluster. (**B**) Comparable

45

829   PSD areas at endbulbs of Held in RIM-BP2 WT and KO. (**C-F**) High magnification (C-E 93,000x; F

830   97,000x) images of IMP-clusters of BC soma facing the endbulb. PSD IMP-clusters indicated by solid

831   black arrow heads. Open black arrow head in F marks the PSD IMP-cluster that lies on the curvature

832   of the synaptic cleft depression and hence was not included in the analysis. All unmarked scale bars

833   are 200 nm. For details about PSD values, sample size and statistics see Table 5.

834

835   A low labelling efficiency for AZ proteins would overestimate the AZ to AZ and $Ca_V2.1$ to AZ particles

836   nearest neighbour distances (NNDs). Hence, we only compared the NND for $Ca_V2.1$ to $Ca_V2.1$ and AZ

837   to $Ca_V2.1$ particles. The value of mean + 2 standard deviations of the Gaussian fit to the distribution

838   of $Ca_V2.1$ to $Ca_V2.1$ NNDs was considered the threshold for the maximum distance by which two

839   particles can be separated and still belong to the same cluster (Fig 9A-B, see materials and methods):

840   mean + 2 s.d. were 43.09 nm and 43.92 nm for WT and RIM-BP2 KO respectively. The threshold used

841   for defining a cluster in our analysis was 40 nm as used in previous analysis (Miki et al., 2017). In many

842   KO AZ images, there were not even three $Ca_V2.1$ gold particles to qualify as a cluster (Fig. 9-2C). Within

843   the qualified clusters, we still found a significantly reduced number of $Ca_V2.1$ particles per cluster in

844   the RIM-BP2 KO (Table 5) which is consistent with a more dispersed $Ca_V2.1$ topography at the AZ as

845   indicated in the STED analysis. To confirm that the clusters obtained in our analysis were valid and

846   not reflecting chance occurrence, we compared our 'real' data to 500 random simulations of cluster

847   arrangements (see materials and methods, and (Luján et al., 2018; Kleindienst et al., 2020)). Table 6

848   confirms the validity of $Ca_V2.1$ clusters and NNDs between $Ca_V2.1$ to $Ca_V2.1$ and AZ to $Ca_V2.1$ particles.

849   The major findings of our FRIL analysis are the significantly lower number and density of $Ca_V2.1$

850   channels as well as the increased AZ to $Ca_V2.1$ NND in RIM-BP2 KO AZs (Fig. 9C, Table 5). There was a

851   trend toward larger $Ca_V2.1$ to $Ca_V2.1$ NND at RIM-BP2 KO AZs which did not reach significance (Fig.

852   9D). The increased AZ to $Ca_V2.1$ NND implies a looser coupling between the Ca^{2+} channels and the AZ

853   proteins likely marking SV release sites.

854

47

855   **Figure 9-2. Similar AZ size but reduced number of AZ and Ca$_V$2.1 labels in endbulbs of RIM-BP2 KO**

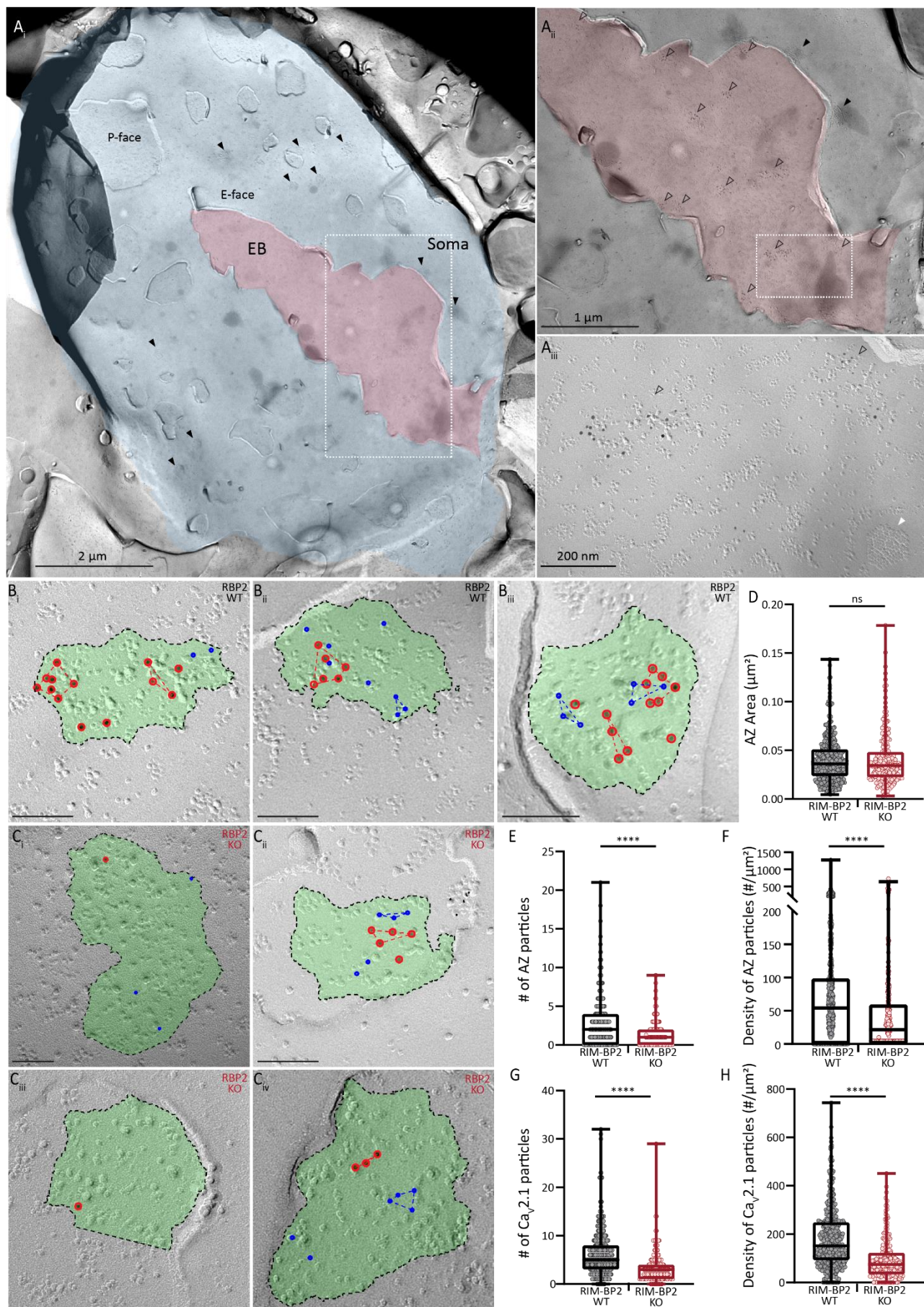**856**   (**A**) SDS-FRIL electron micrograph at low magnification (9700x) showing E-face of a bushy cell (BC)
857   soma (blue) with patches of P-face, connected to an endbulb (red). (**Ai**) Some of the IMP-clusters
858   representing the PSDs of ANF on the BC soma highlighted by solid black arrow heads. (**Aii**) Magnified
859   (18,500x) view of the box in Ai of endbulb synapse (red) on to the BC soma (blue) with IMP-clusters
860   for AZ and PSD indicated by open and solid black arrows respectively. (**Aiii**) Magnified (97,000x) view
861   of the box in Aii with IMP-clusters for AZ indicated by open arrows and P-face of a gap junction
862   indicated by a solid white arrow. (**B-C**) FRIL images showing endbulb AZs (green) in RIM-BP2 WT (B)
863   and KO (C), immunolabelled for AZ molecules (RIM, neurexin, ELKS) and Ca$_V$2.1 channels with 5 nm
864   (blue circles) and 10 nm (red circles) gold particles respectively. (**D-H**) Quantitative analysis of AZ area
865   (**D**), number of AZ (**E**) and Ca$_V$2.1 (**G**) gold particles, and density of AZ (**F**) and Ca$_V$2.1 (**H**) gold particles.
866   All unlabelled scale bars are 100 nm. ns: not significant, **** *p-value* < 0.0001. For details about mean
867   ± SEM, median, sample size and statistics see Table 5.

868

869   **Figure 9. Altered topography of Ca$_V$ channels relative to AZ proteins**

870   (**A-B**) Histogram of nearest neighbor distances (NNDs) between Ca$_V$2.1 to Ca$_V$2.1 gold particles in RIM-
871   BP2 WT (**A**) and KO (**B**). The solid bold line represents Gaussian curve fitted to the NND distribution
872   in RIM-BP 2 WT (black, **A**) and KO (red, **B**). (**C-D**) Cumulative probability of NNDs between AZ to Ca$_V$2.1
873   particles (**C**) and Ca$_V$2.1 to Ca$_V$2.1 particles (**D**) in RIM-BP2 WT (black) and KO (red). ns: not significant,
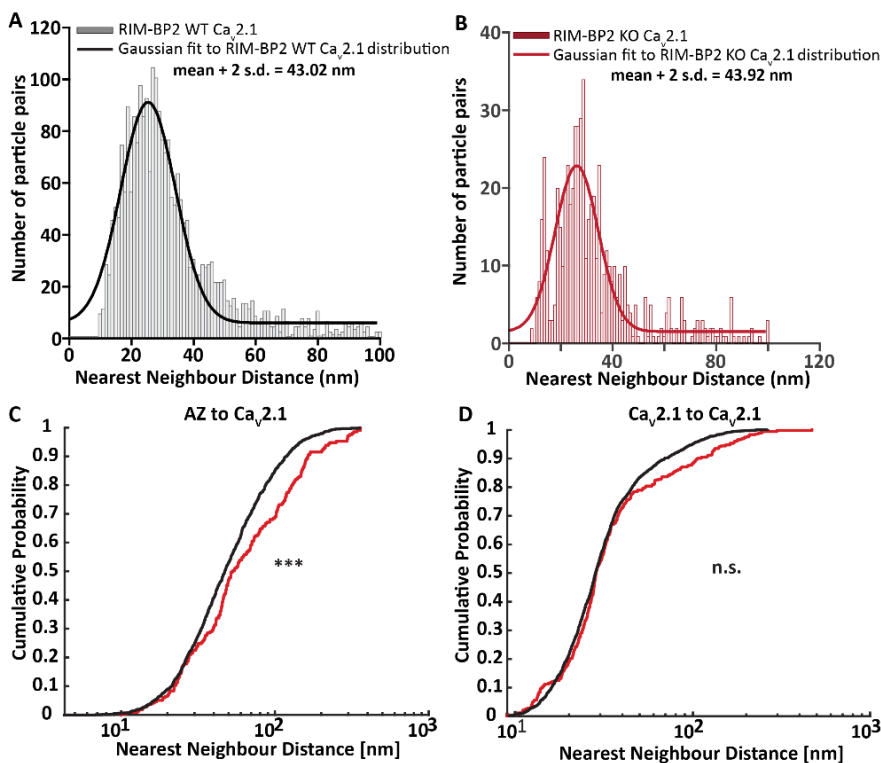**874**   *** *p-value* < 0.001. For details about mean ± SEM, median, sample size and statistics see Table 5.

	Parameter	RIM-BP2 WT	RIM-BP2 KO	p value
	Sample Size			
	# of animals	3	3	-
	# of replicas	6	5	-
	# of images	437	196	-
	# of PSD	136	102	-
	Area Analysis			
	AZ area (μm^2)	0.040 ± 0.001 (0.036)	0.041 ± 0.002 (0.034)	0.75, M
	PSD area (μm^2)	0.026 ± 0.002 (0.022)	0.030 ± 0.003 (0.022)	0.89, M
Gold Particles	**Gold Particle Analysis**			
AZ (5 nm)	# of particles/ AZ area	2.74 ± 0.14 (2.00)	1.34 ± 0.12 (1)	**<0.0001, M**
	Density (#/μm^2)	76.65 ± 4.72 (54.13)	47.91 ± 6.21 (21.41)	**<0.0001, M**
$Ca_V2.1$ (10 nm)	# of particles/ AZ area	6.30 ± 0.22 (5.00)	3.31 ± 0.23 (3.00)	**<0.0001, M**
	Density (#/μm^2)	181.10 ± 5.93 (151.30)	96.88 ± 6.19 (73.72)	**<0.0001, M**
	Cluster Analysis			
$Ca_V2.1$ (10 nm)	# of clusters	342	74	-
	# of particles/cluster	4.36 ± 0.13 (4.00)	3.80 ± 0.16 (3.00)	**0.0011, M**
	Area of cluster (nm^2)	976.25 ± 88.99 (590.90)	659.50 ± 95.37 (418.3)	**0.013, M**
Particle 1 - Particle 2	**Nearest Neighbor Distance (NND) Analysis**			
$Ca_V2.1 - Ca_V2.1$	NND (nm)	37.49 ± 0.57 (28.35)	47.50 ± 2.25 (28.56)	0.05, M
AZ - $Ca_V2.1$	NND (nm)	60.84 ± 1.36 (47.28)	83.64 ± 5.03 (53.16)	**0.0005, M**

875

Table 5 – Quantitative analysis SDS-FRIL electron micrographs

Data were distributed non-normally as determined by Kolmogorov-Smirnov test. Statistical significance of the comparison between RIM-BP2 WT and KO was determined by Mann-Whitney U-Test (denoted in the table as M).

880

881

Genotype	Au Particles	Parameter	Real Data	Simulated Data	p value
		Sample Size			
		# of animals	3	3	-
		# of replicas	6	5	-
		# of images	437	196	-
		Cluster Analysis			
RIM-BP2 KO	AZ (5 nm)	# of clusters/AZ	0.08 ± 0.02	0.05 ± 0.01	0.015
		# of particles/cluster	4.33 ± 0.43	3.71 ± 0.33	0.006
		Area of cluster (nm^2)	759.82 ± 186.11	542.89 ± 125.05	0.09
	Ca$_V$2.1 (10 nm)	# of clusters/AZ	0.38 ± 0.04	0.15 ± 0.02	6.13 e-13
		# of particles/cluster	3.80 ± 0.16	3.35 ± 0.06	0.0003
		Area of cluster (nm^2)	659.50 ± 95.37	438.90 ± 29.90	0.005
Particle 1 - Particle 2	Particle 1 - Particle 2	**Nearest Neighbor Distance (NND) Analysis**			
WT	Ca$_V$2.1 - Ca$_V$2.1	NND (nm)	42.13 ± 1.29	55.20 ± 1.05	5.87 e-28
RIM-BP2 KO	Ca$_V$2.1 - Ca$_V$2.1	NND (nm)	58.14 ± 5.25	85.91 ± 4.80	1.84 e-06

882

Table 6 – Comparison of Real and simulated distribution of gold particles
Real data were compared with 500 random and fitted (only NND analysis) simulations to confirm that the observed clusters and NND distribution are significantly different from chance (random) occurrence.

887

RIM-BP2 disruption alters the SV organization at the endbulb active zones

Next, we high pressure froze aVCNs slices, acutely prepared as for physiology in order to best relate

structure and function, for electron tomography analysis of SV organization at the endbulb AZ.

Following freeze-substitution, embedding, sectioning and tomography, we rigorously analysed and

reconstructed AZ of RIM-BP2 deficient and WT endbulb synapses (Fig. 10). The AZ area, approximated

from the extent of the postsynaptic density, was significantly larger in RIM-BP2-deficient endbulbs

(Fig. 10C & Table 7, $p < 0.01$, Student's t-test). The number (Fig. 10D) and density (Fig. 10E) of SVs per

895   AZ were not altered. For a more comprehensive analysis we compared the SV distribution within 200

896   nm of the presynaptic AZ membrane (perpendicular to the presynaptic membrane into the cytosol of

897   the presynaptic terminal) in 20 nm bins. Morphologically docked SVs (0-2 nm distance), analyzed

898   separately, were significantly fewer in number at RIM-BP2 KO AZs. Significantly fewer SVs were also

899   found for non-docked membrane proximal SVs (2 to 20 nm) and SVs within 40 to 60 nm from the AZ

900   membrane (Fig 10F, *p < 0.01*, Wilcoxon rank test, Table 7). We also analysed top-views of the AZs

901   showing only the docked SVs in the models generated from the tomograms and quantified the

902   percentage of AZs with zero to eight docked SVs. We found that 50% of the analysed RIM-BP2 KO AZs

903   showed zero docked SVs, while two docked SVs per AZ were most frequently encountered in WT (27%

904   of the AZs, Fig. 10G). We further tested for effects of RIM-BP2 disruption on the lateral distribution

905   of the docked SVs by setting a central point within the generated top views and quantifying the

906   distances of all docked SVs from the center (we note that the AZ area captured in the tomograms

907   might not necessarily allow proper definition of the AZ center). The docked SVs appeared to be

908   further away from the center in RIM-BP2 KO synapses, possibly representing a broader distribution

909   over the whole AZs area (Fig. 10J). To analyse the membrane proximal SVs in more detail, we

910   quantified the proportion of SVs in the 2-20 nm bin and observed a shift towards fewer SVs at mutant

911   AZs. Whereas most of the WT (15%) AZs contained 6 SVs within 2-20 nm from the AZ membrane,

912   most mutant AZs showed only 2 or 5 SVs within this distance (Fig. 10K). Lastly, by measuring the

913   diameter of SVs, we found that they exhibited comparable sizes at RIM-BP2 KO and RIM-BP2 WT

914   endbulb AZs (WT: 51.94 ± 0.55 nm; KO: 52.67 ± 0.54 nm). We conclude that RIM-BP2 contributes to

915   normal SV docking and SV organization in close proximity to the membrane of the presynaptic AZ.

916   These changes seem compatible with the lower number of super-primed SVs, impaired SV

917   replenishment (Figs. 3 and 7) and the reduced release probability (Fig. 3).
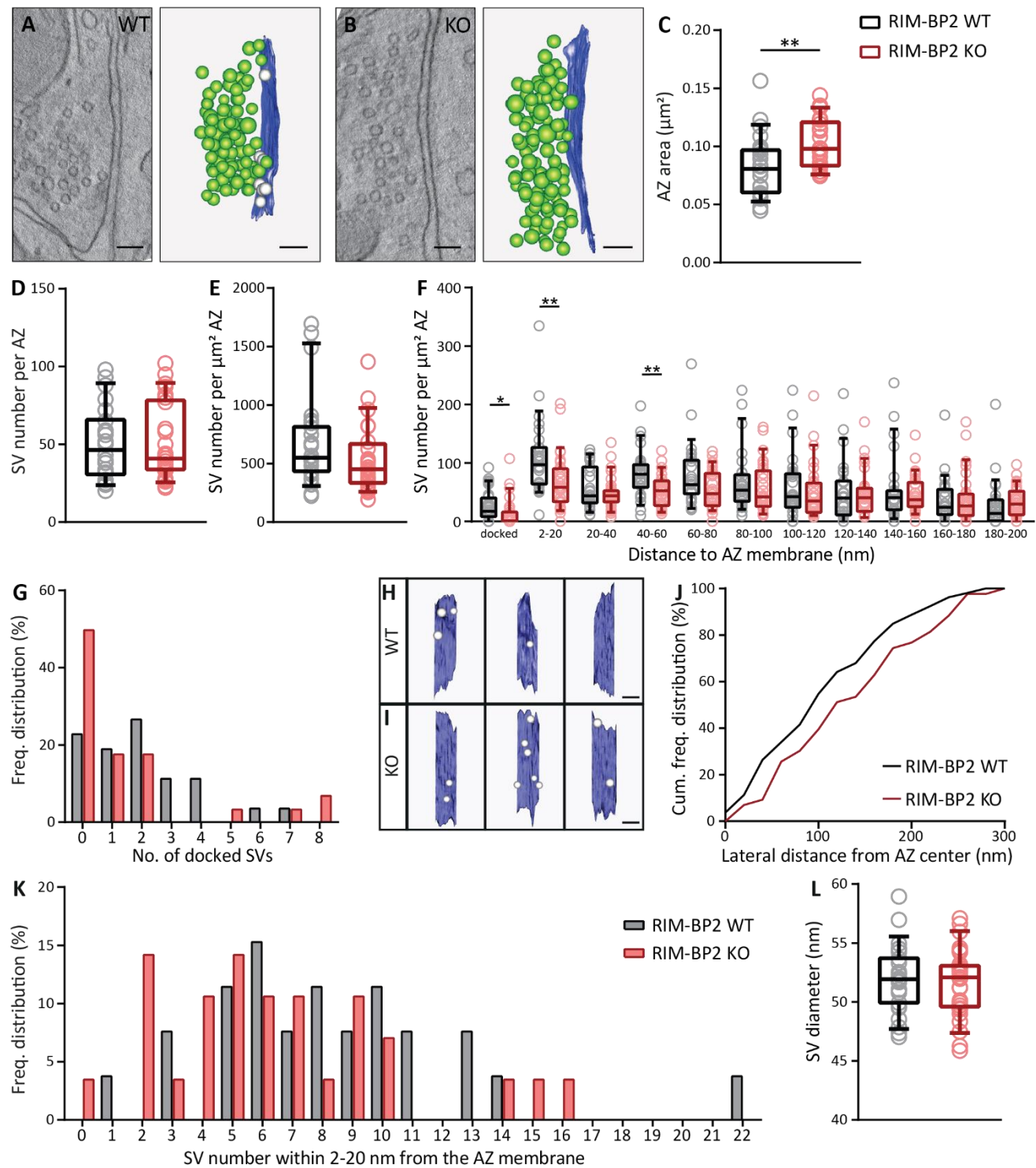
Figure 10. RIM-BP2 disruption alter the axial SV distribution at the endbulb active zones

(**A, B**) Single virtual sections and corresponding models of representative tomograms of RIM-BP2 WT (**A**) and KO (**B**) active zones (AZs) showing the AZ membrane (blue), synaptic vesicles (SVs) (green),

923   and morphologically docked SVs (gray). Scale bars: 100 nm. (**C**) The AZ area estimated by the PSD,

924   was significantly larger in the KO endbulb synapses. **p-value < 0.01, Student's t test. Each data point

925   represents the AZ area of individual synapses. (**D**) Unaltered total number of SVs in mutant AZs. *p-*

926   *value* > 0.05, Student's t test. Each data point represents the number of SVs per AZ of individual

927   synapses. (**E**) SV number normalized to the AZ area is unaltered in KO endbulb AZs. *p-value* > 0.05,

928   Wilcoxon rank test. Each data point represents the number of SVs normalized to the AZ area of

929   individual synapses. (**F**) The number of morphologically docked SVs (0-2 nm) and SVs within 200 nm

930   from the AZ membrane normalized to the AZ area divided into 20 nm bins. *p-value < 0.05, **p-value*

931   < 0.01, Wilcoxon rank test. Each data point represents the number of SVs in each bin normalized to

932   the AZ area of individual AZs. (**G**) Frequency distribution of the number of morphologically docked

933   SVs. (**H,I**) Top views of representative tomogram models of RIM-BP2 WT (**H**) and KO (**I**) AZs with

934   docked SVs. Scale bars: 100 nm. (**J**) Cumulative distribution of the lateral distances of morphologically

935   docked SVs to the assumed center of the reconstructed AZ. (**K**) Frequency distribution of the SV

936   number within 2-20 nm from the AZ membrane. (**L**) Mean SV diameter is unaltered in mutant

937   synapses. *p-value* > 0.05, Student's t test. Each data point represents the mean diameter of SVs of

938   individual synapses. Box and whisker plots present median, lower/upper quartiles, 10–90th

939   percentiles. RIM-BP2-WT (N = 4; n = 26) in black and RIM-BP2-KO (N = 3; n = 28) in red (N, number of

940   animals; n, number of AZs). For details about mean ± SEM, median, and statistics see Table 7.

Parameter		RBP2 WT	RBP2 KO	p value
AZ area (µm^2)		0.0820 ± 0.0052 (0.0809)	0.1031 ± 0.0039 (0.0981)	**0.0022, T**
No. of SVs		49.81 ± 4.49 (46.50)	51.57 ± 4.63 (41.00)	0.79, T
No. of SVs per µm^2 AZ	all SVs	662.3 ± 77.4 (543.1)	523.7 ± 53.4 (443.2)	0.14, W
	docked SVs	27.52 ± 5.24 (18.58)	14.64 ± 4.77 (1.72)	**0.015, W**
	2-20 nm	109.1 ± 12.8 (98.4)	68.16 ± 9.22 (59.32)	**0.006, W**
	20-40 nm	58.59 ± 7.14 (45.26)	49.68 ± 5.40 (45.20)	0.61, W
	40-60 nm	83.25 ± 8.23 (82.21)	53.59 ± 5.36 (53.69)	**0.004, W**
	60-80 nm	79.81 ± 10.62 (64.31)	55.80 ± 6.26 (48.54)	0.09, W
	80-100 nm	70.43 ± 10.52 (54.67)	59.51 ± 7.92 (43.09)	0.39, W
	100-120 nm	61.41 ± 11.08 (43.38)	51.56 ± 9.16 (36.31)	0.51, W
	120-140 nm	50.51 ± 10.47 (41.23)	48.79 ± 7.41 (41.68)	0.64, W
	140-160 nm	55.12 ± 11.25 (42.14)	47.62 ± 6.21 (38.58)	0.82, W
	160-180 nm	37.59 ± 7.70 (25.56)	40.12 ± 8.33 (27.80)	0.92, W
	180-200 nm	29.68 ± 8.40 (15.05)	33.26 ± 4.97 (31.13)	0.20, W
Diameter (nm)	all SVs	50.99 ± 0.59 (51.68)	52.14 ± 0.68 (52.44)	0.73, T

941

942   **Table 7 – Quantitative analysis of electron tomograms**

943   Data are presented as mean ± SEM and medians are shown in parentheses. Normal distribution was

944   assessed with the Jarque-Bera test and equality of variances was assessed with the F-test in normally

945 distributed data. Statistical significance of normally distributed data was determined by unpaired
946 Student's t-test (denoted as T), while that of the non-normally distributed data was determined by
947 the Wilcoxon Rank test (denoted as W). n.s.: not significant, * p-value < 0.05, ** p-value < 0.01.

948

Discussion

949

950 Priming of SVs, Ca$_V$ function as well as the topography of Ca$_V$ and SV release sites at the AZ, co-

951 determine the probability of SV release in response to the action potential invading the presynaptic

952 terminal. Here, we probed the role of RIM-BP2, thought to serve as molecular linker between Ca$_V$ and

953 release sites, and alternatively in SV priming via Munc13, in synaptic transmission at the endbulb of

954 Held synapse. Using super-resolution immunofluorescence and immuno-electron microscopy we

955 demonstrate that RIM-BP2 disruption alters the topography of Ca$_V$2.1 channels at the AZs. Electron

956 tomography revealed fewer docked and membrane-proximal SVs at the AZ. As a physiological

957 corollary of these structural changes, we found a reduction in the amplitude of evoked EPSCs,

958 reduced release probability, and slowed SV replenishment to the RRP. We postulate that RIM-BP2,

959 likely via interaction with Munc13-1, promotes a 'superprimed' (Taschenberger et al., 2016) or 'tightly

960 docked' (Neher and Brose, 2018) SV state. Moreover, RIM-BP2 organizes the topography of Ca$_V$2.1

961 channels, tightly coupling them to SV release sites.

962 Synaptic transmission at calyceal synapses of the lower auditory pathway shows impressive

963 temporal fidelity. At the first central relay of the auditory pathway, co-incident transmission from

964 endbulbs formed by ANFs drives the postsynaptic BCs at hundreds of Hz and with microsecond

965 precision as required for time-critical neural computations such as in sound localization (Trussell,

966 1999; von Gersdorff and Borst, 2002). Such fidelity is enabled by synergistic adaptations on molecular,

967 synaptic and network levels. In the mouse AVCN, BCs receive input from on average 3-4 endbulbs

968 (Cao and Oertel, 2010; Butola et al., 2017) with approximately 400 excitatory AZs (Nicol and

969 Walmsley, 2002; Mendoza Schulz et al., 2014; Butola et al., 2017). Endbulbs feature a large RRP (Lin

970 et al., 2011) and high release probability (estimates range from 0.2 to 0.7: Oleskevich and Walmsley,

971 2002; Wang and Manis, 2005; Chanda and Xu-Friedman, 2010; Mendoza Schulz et al., 2014; Butola

972   et al., 2017) which enable massive synchronous parallel release for powerful excitation of BCs. RIM-

973   BP2 deletion hampers this reliable and temporally precise transmission of auditory information: firing

974   at sound onset was impaired both in rate and temporal precision (Fig. 5). We mainly attribute the

975   reduced firing at sound onset (40% reduction) to the observed impairment of endbulb transmission

976   ($EPSC_1$ amplitude reduction: 36%, Fig. 1), as the deficit in sound onset coding in RIM-BP2 KO ANF was

977   mild (approximately 10% reduction in peak onset firing rate, (Krinner et al., 2017)) and convergence

978   of ANF inputs to BCs is expected to alleviate consequences of impaired ANF coding for BC firing (Joris

979   et al., 1994; Buran et al., 2010). These results from single-neuron recordings are in good agreement

980   with previously reported auditory brainstem responses (Krinner et al., 2017), in which the amplitude

981   reduction was lower for wave I (approximately 30 %) than for wave III (approximately 70%). Wave I

982   and III are attributed to the synchronized firing of ANFs and cochlear nucleus neurons respectively

983   (Melcher et al., 1996). Future studies, also employing analysis of gap detection or sound localization

984   should evaluate the behavioural consequences of this temporal processing deficit.

985   Impaired transmission of sound onset information at RIM-BP2-deficient endbulbs is primarily

986   rooted in a nearly halved initial release probability, which could be restored to wildtype levels upon

987   increasing Ca^{2+} influx (Fig. 7). We attribute the decreased release probability to i) the altered

988   topography of $Ca_V2.1$ and SVs and ii) to the impaired SV docking at RIM-BP2-deficient endbulb AZs.

989   Whole-cell patch-clamp recordings showed normal Ca^{2+} currents in RIM-BP2-deficient endbulbs (Fig.

990   2) and confocal imaging of $Ca_V2.1$ immunofluorescence semi-quantitatively reported a normal Ca^{2+}

991   channel complement of the AZs (Fig. 8-1). This suggests that unlike ribbon synapses (Krinner et al.,

992   2017; Luo et al., 2017), RIM-BP2 is not strictly required for establishing a normal presynaptic Ca_V

993   complement. However, both FRIL and STED imaging of immunolabeled $Ca_V2.1$ channels revealed an

994   impaired clustering of $Ca_V2.1$ at RIM-BP2-deficient endbulb AZs. The number and density of $Ca_V2.1$

995   immunogold particles was reduced at the AZs and the nearest neighboring $Ca_V2.1$ was further away

996   from an immunogold particle marking an AZ protein (Table 5). Nonetheless, distribution of the $Ca_V2.1$

997   immunogold particles was significantly different from random, likely reflecting the presynaptic Ca_V

998   organization by other multi-domain proteins of the AZ such as RIMs (Han et al., 2011; Kaeser et al.,

999   2011; Jung et al., 2015) and CAST (Dong et al., 2018; Hagiwara et al., 2018). Immunofluorescence of

1000 $Ca_V2.1$ as well as of bassoon (marking the presynaptic density) was less confined in space and

1001   immunofluorescent spots were more oval in shape in the absence of RIM-BP2 as compared to

1002   compact, round spots in the WT (Figs. 8 and 8-2). Moreover, the nearest neighboring

1003   immunofluorescence spot was further away both for $Ca_V2.1$ and bassoon. In summary, our data

1004   indicate that RIM-BP2 contributes to orchestrating $Ca_V2.1$ channels at the AZ. Based on our data and

1005   in line with previous studies on other synapses (Liu et al., 2011; Acuna et al., 2015; Brockmann et al.,

1006   2020; Petzoldt et al., 2020), we hypothesize that RIM-BP2 via its interaction with $Ca_V2.1$ and AZ

1007   proteins, contributes to tight coupling of Ca^{2+} channels and vesicular release sites also at the endbulb

1008   of Held synapse. Future experimental and theoretical studies will be needed to further test this

1009   hypothesis.

1010   Recently, an alternative interaction of RIM-BP2 with the C2B domain of Munc13-1 has been

1011   reported by which RIM-BP promotes release probability via SV docking/priming (Brockmann et al.,

1012   2020). The Munc13-1 C2B domain carrying the KW mutation (Shin et al., 2010), showed the highest

1013   affinity for RIM-BP2 binding. Of note, we did not observe a reduction in Munc13-1 or in any other

1014   major AZ protein in our semi-quantitative analysis of AZs in RIM-BP2 deficient endbulbs of Held (Fig.

1015   6). This provides confidence in attributing functional and morphological alterations to the lack of RIM-

1016   BP2 function rather than to quantitative changes in other AZ proteins. Our functional and electron

1017   tomographic analysis of SV pool organization at RIM-BP2-deficient endbulbs now provides evidence

1018   for a role of RIM-BP in SV priming, likely via its interaction with Munc13-1. Rigorous electron

1019   tomography analysis of docking showed nearly halved numbers of morphologically docked SVs

1020   (defined in a distance from 0-2 nm to the AZ membrane) at RIM-BP2-deficient AZs, which might

1021   represent a 'tight docking' (Neher and Brose, 2018). We speculate this to indicate that Munc13-1-

1022   mediated docking that generates primed SVs (Siksou et al., 2009; Imig et al., 2014) partially depends

1023   on the interaction with RIM-BP2. The reduction of both docked SVs and those at a distance of 2-20

1024   nm (membrane proximal SVs) from the plasma membrane might then suggest that the upstream

1025   loose-docking is rate limiting or less stable in the absence of RIM-BP2. An alternative explanation for

1026   retarded recovery from depression might be that RIM-BP2 facilitates release site clearance (Neher

1027   and Sakaba, 2008).

1028   Yet, our analysis of pool dynamics in regular $[Ca^{2+}]_e$ indicated an unaltered RRP size despite

1029   the fact that the numbers of docked and membrane-proximal SVs were nearly halved. Interestingly,

1030   we found a trend toward a smaller RRP in RIM-BP2-deficient endbulbs when restoring release

1031   probability by enhanced Ca^{2+} influx. Despite this partial restoration, the first evoked EPSC amplitude

1032   in the absence of RIM-BP2 was still only 50% of that in the WT synapses (Fig. 7, table 4). This persisting

1033   difference alludes to a deficit in 'super-primed' (Fig. 3, table 2) or 'tightly docked' SVs (Fig. 10, table

1034   7). It is tempting to speculate that the impaired SV docking is uncovered under conditions that

1035   occlude the effect of altered spatial Ca^{2+} channel-release site coupling on release probability. Our

1036   morphological analysis of Ca^{2+} channel-release site coupling is hampered by i) the low number of

1037   docked SVs in electron tomography and ii) the lack of information on the Ca_V position in electron

1038   tomography and of SV docking in FRIL electron micrographs. Nonetheless, there was a trend for

1039   docked SVs to be further away from the estimated AZ center, possibly reflecting a more random SV

1040   topography due to lack of RIM-BP2-mediated interaction with Ca_Vs. In addition, or alternatively, the

58

1041   RRP estimated by SMN/EQ analyses of responses to train stimulation might contain SVs that undergo

1042   tethering, docking and fusion during the train. Recent work by (Pofantis et al., 2021), showed that

1043   deleting the presynaptic protein Mover specifically affects the high P_r component of the RRP at the

1044   Calyx of Held. Pofantis et al. analysed eEPSC trains with non-negative matrix factorization to reveal

1045   components representing sub-pools of SVs with different contributions to transmitter release during

1046   the train. Future studies that tackle how such sub-pools deplete and how they recover from depletion

1047   in synapses lacking both RIM-BP2 as well as RIM-BP2 and Mover will help to further dissect the

1048   contributions of RIM-BP2 to SV super-priming and Ca_V clustering as determinants of P_r.

1049   Exciting topics for future studies include i) the relative contributions of altered Ca^{2+} channel-

1050   release site coupling and impaired SV docking to the reduced release probability, ii) a potential

1051   contribution of release site clearance to the observed deficit in SV docking, and iii) the molecular

1052   mechanisms and structure-function relationship of SV replenishment. Our morphological and

1053   functional experiments indicate that RIM-BP2 takes a role in tethering SVs near the plasma

1054   membrane *en route* to docking. Functionally, the fast, Ca^{2+} dependent component of recovery from

1055   depression due to trains stimulation was hampered. This could reflect a lower local $[Ca^{2+}]$ due to

1056   mislocalization of $Ca_V2.1$ channels. Indeed, a key role of Ca^{2+} in regulating SV replenishment at

1057   calyceal synapses has been reported in multiple studies (Wang and Kaczmarek, 1998; Hosoi et al.,

1058   2007). Interestingly, enhancing Ca^{2+} influx by elevated $[Ca^{2+}]_e$ uncovered a reduced SV replenishment

1059   during train stimulation, which would seem reflect a Ca^{2+} independent limitation e.g. of SV priming.

1060   Future studies on calyceal synapses of mice carrying mutations that target Ca^{2+} dependent effects on

1061   Munc13-1 function and/or the RIM-BP2-Munc13-1 interactions by combined functional and

1062   ultrastructural analyses will be required to elucidate this intricate process. To best relate AZ structure

1063   and function, future studies will ideally employ optogenetic or electric field stimulation followed by

1064   high pressure freezing and EM tomography (Watanabe et al., 2013; Imig et al., 2020 p.202).

1065   **References**

1066   Acuna C, Liu X, Gonzalez A, Südhof TC (2015) RIM-BPs Mediate Tight Coupling of Action Potentials to
1067   Ca2+-Triggered Neurotransmitter Release. Neuron 87:1234–1247.

1068   Acuna C, Liu X, Südhof TC (2016) How to Make an Active Zone: Unexpected Universal Functional
1069   Redundancy between RIMs and RIM-BPs. Neuron 91:792–807.

1070   Brockmann MM, Zarebidaki F, Camacho M, Grauel MK, Trimbuch T, Südhof TC, Rosenmund C (2020)
1071   A Trio of Active Zone Proteins Comprised of RIM-BPs, RIMs, and Munc13s Governs
1072   Neurotransmitter Release. Cell Rep 32:107960.

1073   Buran BN, Strenzke N, Neef A, Gundelfinger ED, Moser T, Liberman MC (2010) Onset coding is
1074   degraded in auditory nerve fibers from mutant mice lacking synaptic ribbons. J Neurosci
1075   30:7587–7597.

1076   Butola T, Wichmann C, Moser T (2017) Piccolo Promotes Vesicle Replenishment at a Fast Central
1077   Auditory Synapse. Front Synaptic Neurosci 9:14.

1078   Cao X-J, Oertel D (2010) Auditory Nerve Fibers Excite Targets Through Synapses That Vary in
1079   Convergence, Strength, and Short-Term Plasticity. Journal of Neurophysiology 104:2308–
1080   2320.

1081   Chanda S, Xu-Friedman MA (2010) A Low-Affinity Antagonist Reveals Saturation and Desensitization
1082   in Mature Synapses in the Auditory Brain Stem. Journal of Neurophysiology 103:1915–1926.

1083   Dittman JS, Ryan TA (2019) The control of release probability at nerve terminals. Nature Reviews
1084   Neuroscience 20:177.

1085   Dolphin AC, Lee A (2020) Presynaptic calcium channels: specialized control of synaptic
1086   neurotransmitter release. Nat Rev Neurosci 21:213–229.

1087   Dong W, Radulovic T, Goral RO, Thomas C, Suarez Montesinos M, Guerrero-Given D, Hagiwara A,
1088   Putzke T, Hida Y, Abe M, Sakimura K, Kamasawa N, Ohtsuka T, Young SM (2018) CAST/ELKS
1089   Proteins Control Voltage-Gated Ca2+ Channel Density and Synaptic Release Probability at a
1090   Mammalian Central Synapse. Cell Rep 24:284-293.e6.

1091   Elmqvist D, Quastel DM (1965) A quantitative study of end-plate potentials in isolated human
1092   muscle. J Physiol 178:505–529.

1093   Gebhart M, Juhasz-Vedres G, Zuccotti A, Brandt N, Engel J, Trockenbacher A, Kaur G, Obermair GJ,
1094   Knipper M, Koschak A, Striessnig J (2010) Modulation of Cav1.3 Ca2+ channel gating by Rab3
1095   interacting molecule. Mol Cell Neurosci 44:246–259.

1096   Grauel MK, Maglione M, Reddy-Alla S, Willmes CG, Brockmann MM, Trimbuch T, Rosenmund T,
1097   Pangalos M, Vardar G, Stumpf A, Walter AM, Rost BR, Eickholt BJ, Haucke V, Schmitz D,
1098   Sigrist SJ, Rosenmund C (2016) RIM-binding protein 2 regulates release probability by fine-
1099   tuning calcium channel localization at murine hippocampal synapses. PNAS 113:11615–
1100   11620.

1101   Gundelfinger ED, Fejtova A (2012) Molecular organization and plasticity of the cytomatrix at the
1102   active zone. Current Opinion in Neurobiology 22:423–430.

1103   Hagiwara A, Kitahara Y, Grabner CP, Vogl C, Abe M, Kitta R, Ohta K, Nakamura K, Sakimura K, Moser
1104   T, Nishi A, Ohtsuka T (2018) Cytomatrix proteins CAST and ELKS regulate retinal
1105   photoreceptor development and maintenance. J Cell Biol 217:3993–4006.

1106   Han Y, Kaeser PS, Südhof TC, Schneggenburger R (2011) RIM Determines Ca2+ Channel Density and
1107   Vesicle Docking at the Presynaptic Active Zone. Neuron 69:304–316.

1108   Hibino H, Pironkova R, Onwumere O, Vologodskaia M, Hudspeth AJ, Lesage F (2002) RIM - binding
1109   proteins (RBPs) couple Rab3 - interacting molecules (RIMs) to voltage - gated Ca2+ channels.
1110   Neuron 34:411–423.

1111   Hosoi N, Sakaba T, Neher E (2007) Quantitative Analysis of Calcium-Dependent Vesicle Recruitment
1112   and Its Functional Role at the Calyx of Held Synapse. The Journal of Neuroscience 27:14286–
1113   14298.

1114   Imig C, López-Murcia FJ, Maus L, García-Plaza IH, Mortensen LS, Schwark M, Schwarze V, Angibaud
1115   J, Nägerl UV, Taschenberger H, Brose N, Cooper BH (2020) Ultrastructural Imaging of
1116   Activity-Dependent Synaptic Membrane-Trafficking Events in Cultured Brain Slices. Neuron
1117   108:843-860.e8.

1118   Imig C, Min S-W, Krinner S, Arancillo M, Rosenmund C, Südhof TC, Rhee J, Brose N, Cooper BH
1119   (2014) The morphological and molecular nature of synaptic vesicle priming at presynaptic
1120   active zones. Neuron 84:416–431.

1121   Isaacson JS, Walmsley B (1995) Receptors underlying excitatory synaptic transmission in slices of the
1122   rat anteroventral cochlear nucleus. Journal of Neurophysiology 73:964–973.

1123   Jing Z, Rutherford MA, Takago H, Frank T, Fejtova A, Khimich D, Moser T, Strenzke N (2013)
1124   Disruption of the presynaptic cytomatrix protein bassoon degrades ribbon anchorage,
1125   multiquantal release, and sound encoding at the hair cell afferent synapse. J Neurosci
1126   33:4456–4467.

1127   Joris PX, Carney LH, Smith PH, Yin TC (1994) Enhancement of neural synchronization in the
1128   anteroventral cochlear nucleus. I. Responses to tones at the characteristic frequency. J
1129   Neurophysiol 71:1022–1036.

1130   Jung S, Oshima-Takago T, Chakrabarti R, Wong AB, Jing Z, Yamanbaeva G, Picher MM, Wojcik SM,
1131   Göttfert F, Predoehl F, Michel K, Hell SW, Schoch S, Strenzke N, Wichmann C, Moser T (2015)
1132   Rab3-interacting molecules 2α and 2β promote the abundance of voltage-gated CaV1.3 Ca2+
1133   channels at hair cell active zones. Proc Natl Acad Sci USA 112:E3141–E3149.

1134   Kaeser PS, Deng L, Wang Y, Dulubova I, Liu X, Rizo J, Südhof TC (2011) RIM proteins tether Ca2+
1135   channels to presynaptic active zones via a direct PDZ-domain interaction. Cell 144:282–295.

1136   Kaeser PS, Regehr WG (2014) Molecular Mechanisms for Synchronous, Asynchronous, and
1137   Spontaneous Neurotransmitter Release. Annual Review of Physiology 76:333–363.

1138   Kiyonaka S, Wakamori M, Miki T, Uriu Y, Nonaka M, Bito H, Beedle AM, Mori E, Hara Y, De Waard M,
1139   Kanagawa M, Itakura M, Takahashi M, Campbell KP, Mori Y (2007) RIM1 confers sustained
1140   activity and neurotransmitter vesicle anchoring to presynaptic Ca2+ channels. Nat Neurosci
1141   10:691–701.

1142   Kleindienst D, Montanaro J, Bhandari P, Case MJ, Fukazawa Y, Shigemoto R (2020) Deep Learning-
1143   Assisted High-Throughput Analysis of Freeze-Fracture Replica Images Applied to Glutamate
1144   Receptors and Calcium Channels at Hippocampal Synapses. International Journal of
1145   Molecular Sciences 21:6737.

1146   Krinner S, Butola T, Jung S, Wichmann C, Moser T (2017) RIM-Binding Protein 2 Promotes a Large
1147   Number of CaV1.3 Ca2+-Channels and Contributes to Fast Synaptic Vesicle Replenishment at
1148   Hair Cell Active Zones. Front Cell Neurosci 11:334.

1149   Lin K-H, Oleskevich S, Taschenberger H (2011) Presynaptic Ca2+ influx and vesicle exocytosis at the
1150   mouse endbulb of Held: a comparison of two auditory nerve terminals. J Physiol (Lond)
1151   589:4301–4320.

1152   Liu KSY, Siebert M, Mertel S, Knoche E, Wegener S, Wichmann C, Matkovic T, Muhammad K, Depner
1153   H, Mettke C, Bückers J, Hell SW, Müller M, Davis GW, Schmitz D, Sigrist SJ (2011) RIM-
1154   binding protein, a central part of the active zone, is essential for neurotransmitter release.
1155   Science 334:1565–1569.

1156   Luján R, Aguado C, Ciruela F, Cózar J, Kleindienst D, de la Ossa L, Bettler B, Wickman K, Watanabe M,
1157   Shigemoto R, Fukazawa Y (2018) Differential association of GABAB receptors with their
1158   effector ion channels in Purkinje cells. Brain Struct Funct 223:1565–1587.

1159   Luo F, Liu X, Südhof TC, Acuna C (2017) Efficient stimulus-secretion coupling at ribbon synapses
1160   requires RIM-binding protein tethering of L-type Ca $^{2+}$ channels. Proceedings of the National
1161   Academy of Sciences 114:E8081–E8090.

1162   Melcher JR, Guinan Jr JH, Knudson IM, Kiang NYS (1996) Generators of the brainstem auditory
1163   evoked potential in cat II. Correlating lesion sites with waveform changes. Hearing research
1164   93:28–51.

1165 Mendoza Schulz A, Jing Z, Sánchez Caro JM, Wetzel F, Dresbach T, Strenzke N, Wichmann C, Moser T
1166   (2014) Bassoon-disruption slows vesicle replenishment and induces homeostatic plasticity at
1167   a CNS synapse. EMBO J 33:512–527.

1168 Miki T, Kaufmann WA, Malagon G, Gomez L, Tabuchi K, Watanabe M, Shigemoto R, Marty A (2017)
1169   Numbers of presynaptic Ca2+ channel clusters match those of functionally defined vesicular
1170   docking sites in single central synapses. Proc Natl Acad Sci U S A 114:E5246–E5255.

1171 Moser T, Grabner CP, Schmitz F (2019) Sensory processing at ribbon synapses in the retina and the
1172   cochlea. Physiol Rev 100:103–144.

1173 Nakamura Y, Harada H, Kamasawa N, Matsui K, Rothman JS, Shigemoto R, Silver RA, DiGregorio DA,
1174   Takahashi T (2015) Nanoscale distribution of presynaptic Ca(2+) channels and its impact on
1175   vesicular release during development. Neuron 85:145–158.

1176 Neher E (2015) Merits and Limitations of Vesicle Pool Models in View of Heterogeneous Populations
1177   of Synaptic Vesicles. Neuron 87:1131–1142.

1178 Neher E, Brose N (2018) Dynamically Primed Synaptic Vesicle States: Key to Understand Synaptic
1179   Short-Term Plasticity. Neuron 100:1283–1291.

1180 Neher E, Sakaba T (2008) Multiple roles of calcium ions in the regulation of neurotransmitter
1181   release. Neuron 59:861–872.

1182 Nicol MJ, Walmsley B (2002) Ultrastructural basis of synaptic transmission between endbulbs of
1183   Held and bushy cells in the rat cochlear nucleus. The Journal of Physiology 539:713.

1184 Oleskevich S, Walmsley B (2002) Synaptic transmission in the auditory brainstem of normal and
1185   congenitally deaf mice. The Journal of Physiology 540:447–455.

1186 Pangrsic T, Singer JH, Koschak A (2018) Voltage-Gated Calcium Channels: Key Players in Sensory
1187   Coding in the Retina and the Inner Ear. Physiological Reviews 98:2063–2096.

1188 Petzoldt AG et al. (2020) RIM-binding protein couples synaptic vesicle recruitment to release sites.
1189   Journal of Cell Biology 219:e201902059.

1190 Picher MM, Oprişoreanu A-M, Jung S, Michel K, Schoch S, Moser T (2017) Rab Interacting Molecules
1191   2 and 3 Directly Interact with the Pore-Forming CaV1.3 Ca2+ Channel Subunit and Promote
1192   Its Membrane Expression. Front Cell Neurosci 11 Available at:
1193   http://www.ncbi.nlm.nih.gov/pmc/articles/PMC5462952/ [Accessed July 3, 2017].

1194 Pofantis E, Neher E, Dresbach T (2021) Regulation of a subset of release-ready vesicles by the
1195   presynaptic protein Mover. Proc Natl Acad Sci U S A 118.

1196 Rubio ME, Matsui K, Fukazawa Y, Kamasawa N, Harada H, Itakura M, Molnár E, Abe M, Sakimura K,
1197   Shigemoto R (2017) The number and distribution of AMPA receptor channels containing fast
1198   kinetic GluA3 and GluA4 subunits at auditory nerve synapses depend on the target cells.
1199   Brain Struct Funct 222:3375–3393.

1200   Sakaba T, Neher E (2001) Quantitative Relationship between Transmitter Release and Calcium
1201   Current at the Calyx of Held Synapse. The Journal of Neuroscience 21:462–476.

1202   Schlüter OM, Basu J, Südhof TC, Rosenmund C (2006) Rab3 superprimes synaptic vesicles for
1203   release: implications for short-term synaptic plasticity. J Neurosci 26:1239–1246.

1204   Schneggenburger R, Meyer AC, Neher E (1999) Released Fraction and Total Size of a Pool of
1205   Immediately Available Transmitter Quanta at a Calyx Synapse. Neuron 23:399–409.

1206   Schneggenburger R, Rosenmund C (2015) Molecular mechanisms governing Ca(2+) regulation of
1207   evoked and spontaneous release. Nat Neurosci 18:935–941.

1208   Sclip A, Acuna C, Luo F, Südhof TC (2018) RIM-binding proteins recruit BK-channels to presynaptic
1209   release sites adjacent to voltage-gated Ca2+-channels. EMBO J 37.

1210   Shin O-H, Lu J, Rhee J-S, Tomchick DR, Pang ZP, Wojcik SM, Camacho-Perez M, Brose N, Machius M,
1211   Rizo J, Rosenmund C, Südhof TC (2010) Munc13 C2B domain is an activity-dependent Ca2+
1212   regulator of synaptic exocytosis. Nat Struct Mol Biol 17:280–288.

1213   Siksou L, Varoqueaux F, Pascual O, Triller A, Brose N, Marty S (2009) A common molecular basis for
1214   membrane docking and functional priming of synaptic vesicles. European Journal of
1215   Neuroscience 30:49–56.

1216   Strenzke N, Chakrabarti R, Al-Moyed H, Müller A, Hoch G, Pangrsic T, Yamanbaeva G, Lenz C, Pan K-
1217   T, Auge E, Geiss-Friedlander R, Urlaub H, Brose N, Wichmann C, Reisinger E (2016) Hair cell
1218   synaptic dysfunction, auditory fatigue and thermal sensitivity in otoferlin Ile515Thr mutants.
1219   EMBO J 35:e201694564.

1220   Südhof TC (2012) The Presynaptic Active Zone. Neuron 75:11–25.

1221   Taberner AM, Liberman MC (2005) Response Properties of Single Auditory Nerve Fibers in the
1222   Mouse. J Neurophysiol 93:557–569.

1223   Taschenberger H, Woehler A, Neher E (2016) Superpriming of synaptic vesicles as a common basis
1224   for intersynapse variability and modulation of synaptic strength. Proc Natl Acad Sci USA
1225   113:E4548–E4557.

1226   Thanawala MS, Regehr WG (2013) Presynaptic Calcium Influx Controls Neurotransmitter Release in
1227   Part by Regulating the Effective Size of the Readily Releasable Pool. J Neurosci 33:4625–
1228   4633.

1229   Trussell LO (1999) Synaptic mechanisms for coding timing in auditory neurons. Annu Rev Physiol
1230   61:477–496.

1231   von Gersdorff H, Borst JGG (2002) Short-term plasticity at the calyx of held. Nat Rev Neurosci 3:53–
1232   64.

1233   Walter AM, Böhme MA, Sigrist SJ (2018) Vesicle release site organization at synaptic active zones.
1234   Neurosci Res 127:3–13.

1235   Wang L-Y, Kaczmarek LK (1998) High-frequency firing helps replenish the readily releasable pool of
1236   synaptic vesicles. Nature 394:384–388.

1237   Wang Y, Manis PB (2005) Synaptic Transmission at the Cochlear Nucleus Endbulb Synapse During
1238   Age-Related Hearing Loss in Mice. J Neurophysiol 94:1814–1824.

1239   Wang Y, O'Donohue H, Manis P (2011) Short-term plasticity and auditory processing in the ventral
1240   cochlear nucleus of normal and hearing-impaired animals. Hearing Research 279:131–139.

1241   Watanabe S, Rost BR, Camacho-Pérez M, Davis MW, Söhl-Kielczynski B, Rosenmund C, Jorgensen
1242   EM (2013) Ultrafast endocytosis at mouse hippocampal synapses. Nature 504:242–247.

1243   Wu SH, Oertel D (1984) Intracellular injection with horseradish peroxidase of physiologically
1244   characterized stellate and bushy cells in slices of mouse anteroventral cochlear nucleus. J
1245   Neurosci 4:1577–1588.

1246   Yang H, Xu-Friedman MA (2008) Relative Roles of Different Mechanisms of Depression at the Mouse
1247   Endbulb of Held. Journal of Neurophysiology 99:2510–2521.

1248   Yu W-M, Goodrich LV (2014) Morphological and physiological development of auditory synapses.
1249   Hearing Research 311:3–16.

1250